LABLE

A Multi-Institutional, Student-Led, Atmospheric Boundary Layer Experiment

BY P. KLEIN, T. A. BONIN, J. F. NEWMAN, D. D. TURNER, P. B. CHILSON, C. E. WAINWRIGHT, W. G. BLUMBERG, S. MISHRA, M. CARNEY, E. P. JACOBSEN, S. WHARTON, AND R. K. NEWSOM

LABLE was a unique, multiphase, low-cost, and multiagency collaboration that provided new insights into boundary layer processes and in which graduate students served as principal investigators.

The atmospheric boundary layer (ABL) is the lowest level of the troposphere that is directly influenced by interactions with the surface of Earth. Over land, it has a marked diurnal cycle due to the diurnal heating and cooling of the land surface (Stull 1988). Accurate predictions of ABL properties and processes are very important for a variety of applications including weather forecasting, air quality studies, public health, and wind energy (Fernando and Weil 2010; Banta et al. 2013; Holtslag et al. 2013; Hu et al. 2013a,b,c; Klein et al. 2014). During daytime, a well-mixed convective boundary layer (CBL) develops, which can be several kilometers deep. Within the CBL, turbulence covers a wide range of scales extending from kilometers for the large energy-containing eddies down to millimeters for the smallest dissipative eddies (Wyngaard 2010). During the early evening transition (EET), the ABL structure changes quickly and becomes more complex than during the daytime (Acevedo and Fitzjarrald 2001). As the surface cools because of radiative heat losses and lack of solar heating, turbulence decays rapidly, and a stable thermal stratification develops in a layer close to the ground: the stable boundary layer (SBL) is being formed. Flow characteristics similar to the CBL from the previous day often persist in the region between the SBL and the capping inversion, which is why this layer is called the residual layer. The multilayer structure of the nocturnal boundary layer (NBL) poses challenges for both the observation and modeling communities (Fernando and Weil 2010; Baklanov et al. 2011; Holtslag et al. 2013; Hu et al. 2013a), and the factors controlling the interactions

AFFILIATIONS: KLEIN, BONIN, NEWMAN, WAINWRIGHT, CARNEY, AND JACOBSEN—School of Meteorology, University of Oklahoma, Norman, Oklahoma; TURNER—NOAA/National Severe Storms Laboratory, Norman, Oklahoma; CHILSON—School of Meteorology, and Advanced Radar Research Center, University of Oklahoma, Norman, Oklahoma; BLUMBERG—School of Meteorology, and Cooperative Institute for Mesoscale Meteorological Studies, University of Oklahoma, Norman, Oklahoma; MISHRA—Cooperative Institute for Mesoscale Meteorological Studies, University of Oklahoma, Norman, Oklahoma; WHARTON—Lawrence Livermore National Laboratory, Livermore, California; NEWSOM—Pacific Northwest National Laboratory, Richland, Washington
CORRESPONDING AUTHOR: Dr. Petra Klein, School of Meteorology, University of Oklahoma, 120 David L. Boren Blvd., Norman, OK 73072
E-mail: pkklein@ou.edu

The abstract for this article can be found in this issue, following the table of contents.

DOI:10.1175/BAMS-D-13-00267.1

In final form 3 December 2014

between the SBL and residual layer are currently not well understood. Under many circumstances, the turbulent exchange between the residual layer and the SBL is limited, and the residual layer becomes decoupled from the SBL (Mahrt 1999, 2014). This situation may be altered by the presence of a nocturnal low-level jet (LLJ) or mesoscale disturbances.

The LLJ is an ABL phenomenon that is commonly observed over the Great Plains of the United States (e.g., Blackadar 1957; Bonner 1968; Parish et al. 1988; Mitchell et al. 1995; Stensrud 1996; Zhong et al. 1996; Whiteman et al. 1997; Banta et al. 2002; Song et al. 2005; Walters et al. 2008) and at other locations worldwide (e.g., Beyrich et al. 1997; Baas et al. 2009). The jet typically begins to develop around sunset, under dry cloud-free conditions conducive to strong radiative cooling, reaching its peak intensity toward the end of the night, and then decaying after dawn with the onset of daytime convective mixing. The wind maximum typically occurs at levels less than 1 km above ground and frequently happens within the lowest 500 m. The peak LLJ wind speeds are often supergeostrophic by approximately 70% but can exceed the geostrophic values by several hundred percent in strong cases (e.g., Hoecker 1963; Bonner 1968; Brook 1985). The vertical wind distribution in an LLJ typically has a distinctive shape characterized by a pronounced wind maximum, often referred to as the LLJ nose. Despite the presence of strong shear associated with these LLJs, turbulent transport below the wind maximum may be inhibited because of the damping effect of stable stratification on turbulence production; however, there are cases where the turbulence levels remain high or the turbulence is intermittent (Banta et al. 2006). Characterizing the complex nature of the NBL structure and turbulence was one of the motivations for LABLE.

To better understand the dynamic and thermodynamic structure of the ABL, high temporal resolution profiles of mean and turbulent quantities of wind, temperature, humidity, and other trace gases throughout the entire ABL depth are needed (NRC 2009, 2010). Recent studies have highlighted the skill of ground-based remote sensing instrumentation in providing reliable observations of wind, temperature, and humidity profiles in the ABL (Wang et al. 2007; Newsom et al. 2008; Banta 2008; Friedrich et al. 2012; Banta et al. 2013; Barthelmie et al. 2014; Turner and Löhnert 2014). However, questions concerning the accuracy of remotely sensed ABL parameters remain, the collected datasets are often limited, and the interactions of ABL processes with synoptic-scale conditions, orography, and land surface characteristics are still not well understood. To provide new insights into spatial and temporal variations of turbulent processes within the ABL, LABLE combined instruments of different operating principles, temporal and spatial resolutions, and sensitivities and assessed their accuracy against in situ observations. The complementary vertical resolution and range of the various instruments provided a near-complete picture of the thermodynamic, dynamic, and turbulence structure of the ABL at spatial and temporal resolutions, which was, to our knowledge, not met in previous studies.

The LABLE experiments had four primary scientific objectives: 1) to compare observations of mean and turbulent motions from Doppler wind lidars and sodars and to characterize their mean accuracy and sensitivity over a range of different environmental conditions (e.g., CBL vs SBL, high– vs low–wind speed conditions), 2) to assess the accuracy and reliability of temperature profiles measured with the Atmospheric Emitted Radiance Interferometer (AERI), 3) to obtain a better understanding of the structure and turbulent processes within the NBL and their interaction with larger-scale weather patterns, and 4) to investigate how turbulent statistics, such as variance and skewness profiles of vertical motions, vary with upwind land surface conditions. Another unique objective of LABLE was to provide experience for graduate students in observational ABL studies covering all aspects from the design of a field campaign to the scientific analysis of the collected datasets. The goal of this paper is to provide an overview of the LABLE campaigns and the types of data collected. The results presented focus on the first three goals mentioned above. Naturally, the LABLE observations can be used for a range of different studies, and ideas for future analyses are discussed in the conclusions and outlook.

LABLE CAMPAIGNS. The two LABLE field campaigns were organized and conducted by the Boundary Layer Integrated Sensing and Simulation (BLISS) group at the National Weather Center (NWC) in Norman, Oklahoma. The BLISS group brings together graduate students, professors, and scientists from the School of Meteorology at the University of Oklahoma (OU) and from NOAA's National Severe Storms Laboratory (NSSL). It facilitates interagency coordination of research and education efforts in boundary layer meteorology, as well as the integration of in situ and remote sensing instrumentation with numerical modeling techniques. The two LABLE campaigns were designed as low-cost experiments that leveraged existing instrumentation and ongoing collaborations with the Department of Energy's Atmospheric Radiation Measurement (ARM) Program (Mather and Voyles

2013) and Lawrence Livermore National Laboratory (LLNL). Weekly meetings of the BLISS group served as a platform for developing the general deployment strategies for the two campaigns. Graduate students served as principal investigators, playing a leading role in the experiment design, the day-to-day operation of the various instruments, and the data acquisition and storage, quality assurance, and scientific analysis of the collected datasets. The experimental design of the LABLE I campaign, which ran from 18 September to 13 November 2012, was more driven by the scientific objectives outlined by senior personnel, although the graduate students were able to provide input and gained useful experience in the deployment and operation of the instruments. During the weekly BLISS meetings, updates were given about the status of the various instruments and data streams, and possible changes to the experimental plan were discussed. Graduate students also developed scripts to integrate different data streams and to create quick-look plots that allowed assessing the data quality in near–real time. For LABLE II, which was from 12 June to 3 July 2013, two Ph.D. students independently developed specific DL deployment and scanning strategies to obtain datasets that are essential for their Ph.D. research. With the experience gained during LABLE I, the students were able to conduct the experiment requiring only minor support from senior personnel.

INSTRUMENTATION AND OBSERVATIONAL STRATEGIES. LABLE was conducted at the ARM Southern Great Plains (SGP) site, located in north-central Oklahoma in rural terrain with primarily pasture and farmland (Fig. 1a). All LABLE instruments were deployed at the SGP central facility (Fig. 1b) near Lamont (36.606°N, 97.485°W), which is approximately a 2-h drive north of the main OU campus. The SGP central facility operates a wide range of in situ and remote sensing instrumentation for monitoring of the ABL (Mather and Voyles 2013). Of particular interest for LABLE were the ARM Streamline Doppler lidar (DL), 915-MHz wind profiler, water vapor and aerosol Raman lidar, AERI, rawinsonde releases four times per day, and flux observations made by sonic anemometers and infrared gas analyzers at 4 m above ground level (AGL) at an eddy correlation (ECOR) flux measurement system and at 25 and 60 m AGL on a 60-m tower. During the LABLE I campaign, BLISS deployed three additional wind profiling instruments (2 DLs and a sodar); during LABLE II three DLs were deployed. Details about the siting and specifications of all instruments used for the LABLE I and II studies can be found in Fig. 1 and Table 1; Fig. 2 shows photos of the primary LABLE instruments. Data from the 915-MHz radar wind profiler have been compared with DL observations, but these comparisons are not included in this

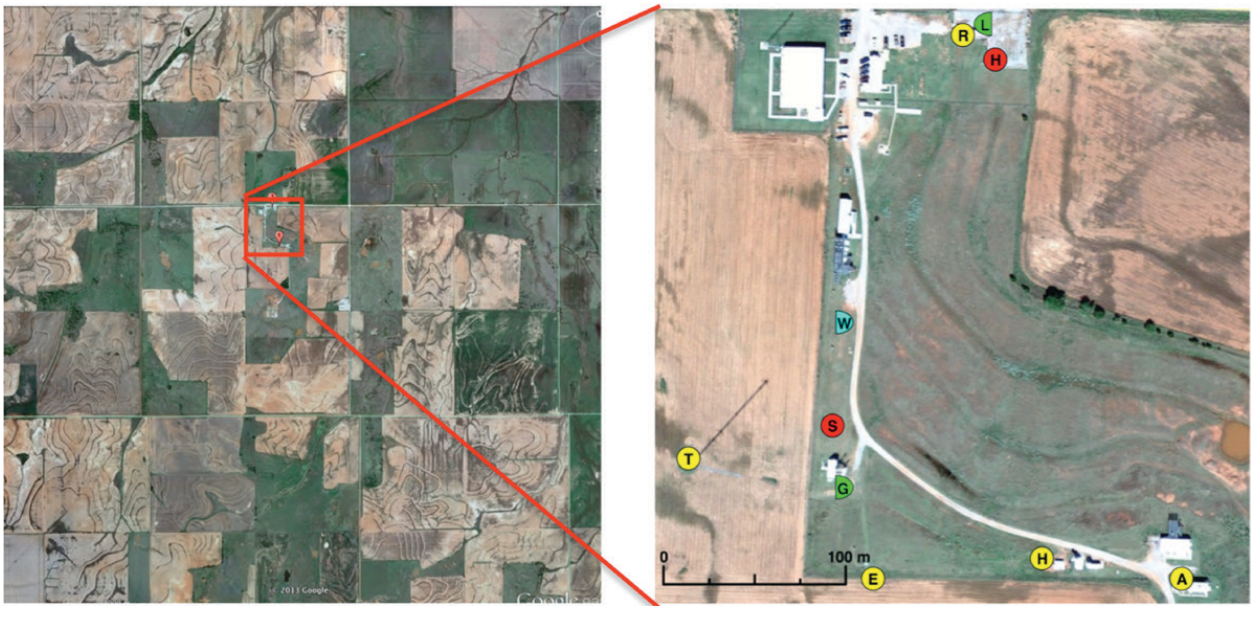

Fig. 1. (left) The domain around the ARM SGP site demonstrating the various surface types (pasture, farmland) in the nearby vicinity and (right) a detailed view of the SGP central facility. Locations of important ARM facilities are highlighted in yellow (60-m tower, T; ECOR system, E; Streamline DL, H; AERI, A; Raman lidar, R), OU instrumentation is shown in red (Metek sodar, S; Streamline DL, H), instruments on loan or rented from vendors are marked in green (Galion DL, G; Leosphere 200s, L), and the teal symbol marks the site of the LLNL DL WINDCUBE v2 (W). (Images from are taken from Google Earth from Sep 2011.)

paper since we primarily focus on the lowest 2 km of the ABL where the resolution of the DL and sodar are superior to the radar wind profiler. Important aspects of the ARM instrumentation utilized for this study are shortly summarized thereafter, before the DL scanning strategies are described in detail.

Raman lidar and AERI. The ARM SGP Raman lidar is an operational system that was designed to measure water vapor, aerosols, and clouds over the diurnal cycle (Goldsmith et al. 1998). The lidar transmits a pulsed laser beam vertically at 355 nm and measures the backscattered photons from Rayleigh–Mie scattering as well as Raman scattering by water vapor and nitrogen molecules. These measurements are used to derive profiles of water vapor mixing ratio, aerosol backscatter, and the extinction coefficient, as well as other geophysical variables (Turner and Goldsmith 1999; Turner et al. 2002). The system was upgraded in 2004 with new detection electronics (Newsom et al. 2009), greatly improving the signal-to-noise ratio in the various products (Ferrare et al. 2006), and new channels to profile temperature (Newsom et al. 2013). The improved capability allows water vapor turbulence profiles in the CBL to be derived from lidar observations (Wulfmeyer et al. 2010; Turner et al. 2014). The AERI is a passive interferometer that measures downwelling infrared radiance from which ABL profiles of temperature and humidity are retrieved (see discussion of the Atmospheric Emitted Radiance Interferometer in the sidebar).

Eddy correlation flux measurements. The combined sonic and infrared gas analyzer measurements at the ARM ECOR system site and 60-m tower collect time series of all three velocity components (u, v, and w), sonic temperature T_s (which is a good measure of virtual temperature), water vapor, and CO_2 densities with a sampling frequency of 10 Hz at 4, 25, and 60 m AGL. Using the eddy covariance approach, 30-min mean estimates of the fluxes of momentum, CO_2, latent heat, and sensible heat are computed from the raw time series applying several quality assurance techniques (Kaimal and Finnigan 1994; Cook 2011). The 10-Hz sonic anemometer data are first passed through a spike filter to eliminate noisy and erroneous data. Data points that are more than a prescribed number of standard deviations away from the 100-s running mean are set to the value of the running mean and are not used in subsequent calculations of the running mean quantities. Before calculating the fluxes, a 2D coordinate rotation is applied, which forces the mean values of v and w to be zero. Webb–Pearmann–Leuning corrections are also applied (Webb et al. 1980; Fischer 2004).

Sodar. During LABLE I, a Metek PCS.2000 sodar owned by OU was operated with an acoustic frequency of 1895 Hz in a Doppler beam-swinging (DBS; Strauch et al. 1984) mode consisting of five beam directions with a zenith angle of 17.8° for the four off-vertical beams. The system completed a five-beam scan every 15 s, and the Doppler spectra were incoherently integrated over a period of 10 min to improve the signal-to-noise ratio (SNR). The maximum possible sensing height of this system was 500 m, and the typical maximum retrieval height during LABLE was approximately 200 m. The percentage of time the sodar was operational during LABLE I is 99.5% (the only time it was turned off was for repair). The sodar observations used in this paper were cluster-analyzed wind component values, which are a direct output from the Metek PCS.2000 sodar. Radial components from instantaneous spectra with sufficiently high SNRs are sorted into classes of width 0.1 m s^{-1}, and cluster identification is performed using a running acceptance window of width 1 m s^{-1}. Averaging the samples within the 1 m s^{-1} window containing the highest overall number of samples identifies the radial velocity. The cluster algorithm for evaluation of instantaneous spectra was performed at the sodar averaging period of 10 min. Only 10-min cluster-analyzed data of the zonal and meridional wind components u and v with an SNR of ≥3 dB were used for wind speed and direction analysis. The 3-dB threshold was chosen, as it is used internally in the sodar software to filter data for the cluster analysis. At a height of 150 m, the SNR was ≥3 dB for the following percentages of time: 59.0% (day), 49.3% (night), and 54.1% (all). For a lower height of 100 m, the equivalent ≥3-dB values are 80.8% (day), 69.2% (night), and 75.0% (all). Here, day and night refer to the time periods 1200–2400 and 0000–1200 UTC, respectively.

Doppler lidars. During LABLE I, there were three DLs operating at the SGP site. The operational ARM Streamline DL and the OU Streamline DL are identical systems (except for the OU instrument having an extended range) that were manufactured by Halo Photonics (Pearson et al. 2009). The vendor Leosphere loaned the third DL, a Leosphere WINDCUBE 200, to NSSL for this experiment. These three commercially available DLs use pulsed 1.5-μm lasers and detect the backscattered energy from aerosol particles in the boundary layer. The percentages of

ATMOSPHERIC EMITTED RADIANCE INTERFEROMETER (AERI)

The Atmospheric Emitted Radiance Interferometer (AERI) is an operational ground-based spectrometer that measures the downwelling infrared (3–19 μm) radiance emitted by the atmosphere at a high temporal and spectral resolution (Knuteson et al. 2004a). These spectra, examples of which are shown in Fig. SB1, provide a wealth of information on the state of the atmosphere above the instrument. Data from the AERI have been used in a wide range of analyses, including for characterizing the evolution of the thermodynamic structure of the lower troposphere (e.g., Feltz et al. 1998; Feltz et al. 2003), quantifying the microphysical properties of clouds (e.g., Mace et al. 1998; Comstock et al. 2007; Turner 2007) and aerosols (e.g., Turner 2008), providing estimates of trace gas concentrations in the column (e.g., Yurganov et al. 2010), and improving the accuracy of spectroscopic radiative transfer models (e.g., Tobin et al. 1999; Turner et al. 2004; Mlawer et al. 2012).

The spectral signature of the downwelling radiance contains information on the vertical profile of temperature and water vapor, as illustrated by the differences among the temperature and water vapor (Fig. SB1c) profiles associated with the three observed spectra (Fig. SB1a). Trace gases such as carbon dioxide, ozone, methane, and, of course, water vapor have many absorption lines in the portion of the infrared spectrum observed by the AERI (Fig. SB1b), and clouds and aerosols are easily observed in the 8–12-μm atmospheric window. Retrieval algorithms, such as the one by Turner and Löhnert (2014), use portions of the observed spectrum to derive information on the atmospheric profiles. The strong carbon dioxide absorption band centered at 15 μm, which is composed of hundreds of absorption lines of various strengths and thus optical depths, provides information on the temperature profile, with AERI channels associated with more opaque absorption features providing information closer to the instrument (i.e., near the surface) and more transparent channels providing information aloft. Similarly, a large number of AERI channels where water vapor is the primary absorbing gas (note that there are many spectral regions where multiple gases absorb radiation simultaneously and these regions are typically not used in retrieval algorithms) are used to provide the profile of water vapor. Clouds are a strong emitter of infrared radiation, and thus retrieval algorithms are built to simultaneously retrieve thermodynamic profiles and cloud properties (e.g., Turner and Löhnert 2014).

As with any ground- or space-based passive remote sensor, accurate calibration is critical, as any bias in the observed radiance results in significant errors in the retrieved atmospheric properties. The AERI regularly views two blackbodies that have well-characterized emissivity characteristics and accurate thermistors embedded to provide a radiometric calibration that is better than 1% of the ambient radiance (Knuteson et al. 2004b). The calibration stability of this instrument not only enables accurate thermodynamic profiling, but also long-term trend analysis of downwelling radiance (Gero and Turner 2011).

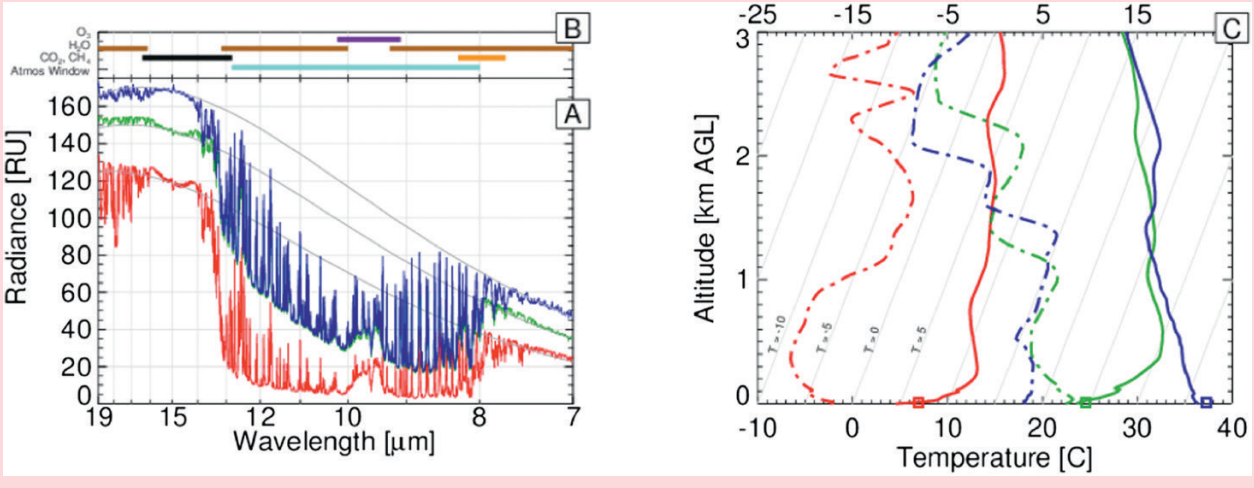

FIG. SB1. AERI-observed downwelling radiance (a) at the SGP site associated with (c) three different atmospheric profiles at 1125 UTC 7 Nov 2012 (red) and at 1132 and 1731 UTC 27 Jun 2013 (green and blue, respectively), where the solid and dashed–dotted lines in (c) are the ambient and dewpoint temperatures, respectively. All three of these cases are cloud free. (b) Shown are the primary absorbing gases in each spectral region. The observed PWVs were 13.2, 36.1, and 35.1 kg m^{-2}, respectively. The surface air temperatures derived from the AERI spectra, which is indicated by the Planck radiance spectra in gray in (a), are denoted as the squares at the base of the profiles in (c) and show good agreement with the rawinsonde observations [please note that in (c) a skewed temperature scale is used].

Table 1. Overview of the instrumentation deployed during the LABLE field campaigns (names of graduate students serving as co–primary investigators (PIs) are italicized in the second column).

Instruments/platform	Owner/operator/deployment	Available data output	Specifications
Gill Solent Windmaster Pro 3D sonic anemometer and Licor Infrared Gas Analyzer/60-m tower and ECOR system*	ARM/Lawrence Berkeley National Laboratory/continuous	30-min averages of V, (WD), T_s, and vertical fluxes of momentum, CO_2, sensible heat, and latent heat**	H = 4, 25, 60 m
			Range: 0 to 65 m s^{-1} (V), −40° to +60°C (T_s)
			Accuracy: 1.5% RMSE for u and v, 3% RMSE for w, 3% error in speed of sound for Ts
			Resolution: 0.01 m s^{-1} (V), 0.02°C (T_s)
			Flux detection limits: CO_2, ~0.1 μmol m^{-2} s^{-1}; gain uncertainty, 1% to 3%; H_2O, ~10 W m^{-2}; gain uncertainty, 1% to 3%; sensible heat, ~10 W m^{-2}; gain uncertainty, 1% to3%
Vaisala HMP45D/60-m tower	ARM/Argonne National Laboratory/ continuous	1-min time series of T and RH	H = 25, 60 m
			Range: −30° to 40°C (T), 0% to 100% (RH)
			Accuracy: ±0.2°C (T), ±2% up to 90% (RH), ±3% above 90% RH
Vaisala 50Y Humitter/ECOR system	ARM/Lawrence Berkeley National Laboratory/continuous	30-min time series of T and RH	H = 2, 3 m
			Range: −10° to 60°C (T), 0% to 100% (RH)
			Accuracy: ±0.6°C (T), from ±2% to ±3% (RH)
AERI	ARM/ARM/continuous	Downwelling IR radiance spectra every 20 s; Retrieved temperature and humidity profiles every 5 min	Spectral range: 520–3000 cm^{-1} at 1.0-cm^{-1} resolution
			Accuracy: better than 1% of the ambient radiance
			Thermodynamic profiling range: surface to ~3 km
			Accuracy of temperature profile: better than 0.5 K
Raman lidar	ARM/ARM/continuous	Backscatter data in multiple channels at 7.5-m, 10-s resolution; water vapor profiles at 75-m, 10-s resolution	Laser wavelength: 0.355 μm
			Pulse repetition rate: 30 Hz
			Accuracy of the water vapor profiles in lowest 4 km: 5% or 0.5 g kg^{-1}, whichever is larger

Table 1. Continued.

Instruments/platform	Owner/operator/deployment	Available data output	Specifications
Vaisala RS92 rawinsondes	ARM/ARM/regularly every 6 h (0000, 0600, 1200, and 1800 UTC)	Vertical profiles of atmospheric pressure p, RH, and T	Range: 0% to 100% (RH), −90° to +60°C (T), 1080 to 3 hPa (p)
		Wind speed and direction determined using GPS	Uncertainty: 5% (RH), 0.5°C (T)
			Resolution: 1% (RH), 0.1°C (T), 0.1 hPa (p)
OU Metek sodar	OU/P. Chilson and *C. Wainwright*/LABLE I	10-min averages of power, SNR, and radial velocities, which are used to calculate 3D wind components	H = 30 to 500 m
			Range resolution: 10 m
			Accuracy—wind direction: ±5°
			Wind speed: ±0.5 m s^{-1} (below 5 m s^{-1}) and ±10% above 5 m s^{-1}
ARM Streamline DL	ARM/Pacific Northwest National Laboratory/continuous	~1-Hz radial velocities, VAD-derived horizontal wind every 15 min, σ_w usually averaged over 30 min	H = 100 to 3000 m
			Range resolution: 30 m
			Range: ±19.4 m s^{-1} (Nyquist velocity)
			Resolution: <20 cm s^{-1} for SNR > −17 dB
			Wavelength: 1.5 μm
			Pulse repetition rate: 15 kHz
OU Streamline DL	OU/P. Klein and *T. Bonin*/LABLE I and II	~1-Hz radial velocities, VAD-derived horizontal wind (frequency varied), σ_w usually averaged over 30 min	H = 100 to 3000 m (technically can collect data out to 9.6 km)
			Range resolution: 18 m
			Range: ±19.4 m s^{-1} (Nyquist velocity)
			Resolution: <20 cm s^{-1} for SNR > −17 dB
			Wavelength: 1.5 μm
			Pulse repetition rate: 15 kHz
Galion DL	SGURR Energy/P. Klein, *T. Bonin*, and *J. Newman*/LABLE II	~1-Hz radial velocities, outputs varied based on different scan strategies during LABLE II	H = 80 to 4000 m
			Range resolution: 30 m
			Range: ±38.8 m s^{-1} (Nyquist velocity)
			Resolution: <20 cm s^{-1} for SNR > −17 dB
			Wavelength: 1.5 μm
			Pulse repetition rate: 15 kHz

Table 1. Continued.

Instruments/platform	Owner/operator/deployment	Available data output	Specifications
Leosphere WINDCUBE 200	Leosphere/D. Turner/LABLE I	Carrier noise ratio (dB), vertical velocity ($m\ s^{-1}$), and vertical dispersion ($m\ s^{-1}$) profiles (this system only stared vertically)	Temporal resolution: 4 s
			Vertical resolution: 50 m
			Resolution: <20 cm s^{-1}
			Wavelength: 1.5 μm
			Pulse repetition rate: 20 kHz
LLNL Leosphere WINDCUBE v2	LLNL/S. Wharton and *J. Newman*/LABLE II	u, v, and w at 1 Hz	H = 40 to 200 m
			Range resolution: 20 m
			Range: ±60 m s^{-1}
			Accuracy: 0.1 m s^{-1}
			Wavelength: 1.5 μm
			Pulse repetition rate: 20 kHz

* The measurements at 4 m AGL are taken at the ECOR system site (E); the 25- and 60-m data are collected at the 60-m tower (T).

** For our analysis, we used a data stream with 30-min-averaged fluxes, which are computed using 10-Hz time series of the wind velocity components u, v, and w; sonic temperature T_s measured by the sonic anemometer; and CO_2 and H_2O densities measured by the infrared gas analyzer. The data stream also includes additional variables such as Obukhov length L and friction velocity u_*.

time the Streamline lidars were up and running during LABLE I are 100% for the ARM Streamline and 85.6% for the OU Streamline. Over the entire day and night at a height of 1000 m, the SNR was greater than –21 dB for 89% of the time for the ARM Streamline and 82.5% for the OU Streamline. The corresponding numbers for the ARM (OU) Streamline systems are 88.6% (82.2%) at night (0000–1200 UTC) and 89.4% (82.8%) during the day (1200–2400 UTC).

During LABLE I, the ARM Streamline DL performed a plan position indicator (PPI) scan at a 60°-elevation angle every 15 min in order to derive horizontal winds using the velocity azimuth display (VAD) technique. These PPI scans used eight azimuthal angles and took approximately 1 min. During the remaining time the ARM Streamline DL collected radial velocities in the zenith direction (i.e., vertical velocities). The OU Streamline DL also performed PPI scans but at both 40° and 70° elevations. The lower elevation angle improved the accuracy of the horizontal winds in low–wind speed conditions and at lower altitudes, whereas the higher elevation angle was selected to improve measurements of the high wind speeds. These PPI scan pairs occurred every 30 min and used 72 azimuthal angles during most of LABLE I. Between the PPI scans, the OU Streamline DL collected vertical velocity data. The Leosphere WINDCUBE 200, which was located directly adjacent to the Raman lidar, only collected vertical velocities to obtain continuous datasets for the analysis of turbulence properties and water vapor fluxes in the ABL.

During LABLE II, we rented a Galion DL from SGURR energy and deployed it along with the OU Streamline DL and a Leosphere WINDCUBE v2, which is owned by LLNL. The Galion DL is nearly identical to the Streamline DLs (Table 1). We focused on testing different scanning strategies with the Galion and two Streamline systems to obtain high-resolution datasets that can provide accurate turbulence statistics for evaluating data collected with commercially available profiling lidars such as the Leosphere WINDCUBE v2, which employs a DBS technique to measure the three-dimensional wind vector. In each WINDCUBE DBS scan, the lidar beam is pointed toward the four cardinal directions at an elevation angle of 62° and then pointed vertically. It takes just under 1 s to collect measurements in each beam direction, such that a full DBS scan is completed approximately every 4 s. However, the WINDCUBE v2 velocity algorithm calculates the u, v, and w components every second using the four preceding radial velocity measurements (Cariou 2011).

Doppler lidar scanning strategies and signal processing. One of the goals of LABLE II was to evaluate different lidar scanning techniques for measuring turbulence. When the DBS technique is used to measure turbulence, three major problems cause the lidar to measure different turbulence values than would a sonic anemometer (e.g., Sathe et al. 2011; Sathe and Mann 2012). The first problem is inherent in all remote sensing technology and involves averaging within the probe volume. In the LABLE experiments, lidar range gates were between 18 and 30 m; thus, turbulence scales smaller than these lengths could not be measured accurately. Next, in order to solve the DBS equations, it must be assumed that the velocity is uniform throughout the scanning circle formed by the various beam positions. For low heights and uniform terrain, this assumption is likely valid at times but becomes invalid for higher measurement heights and complex terrain. Finally, the use of only four off-zenith beams to calculate three-dimensional turbulence introduces systematic errors. Sathe and Mann (2012) show that the calculated variance values of u, v, and w are contaminated by the cross components of the Reynolds stress tensor; that is, the variance of the v component has contributions from not just the v component of the wind but the u and w components as well.

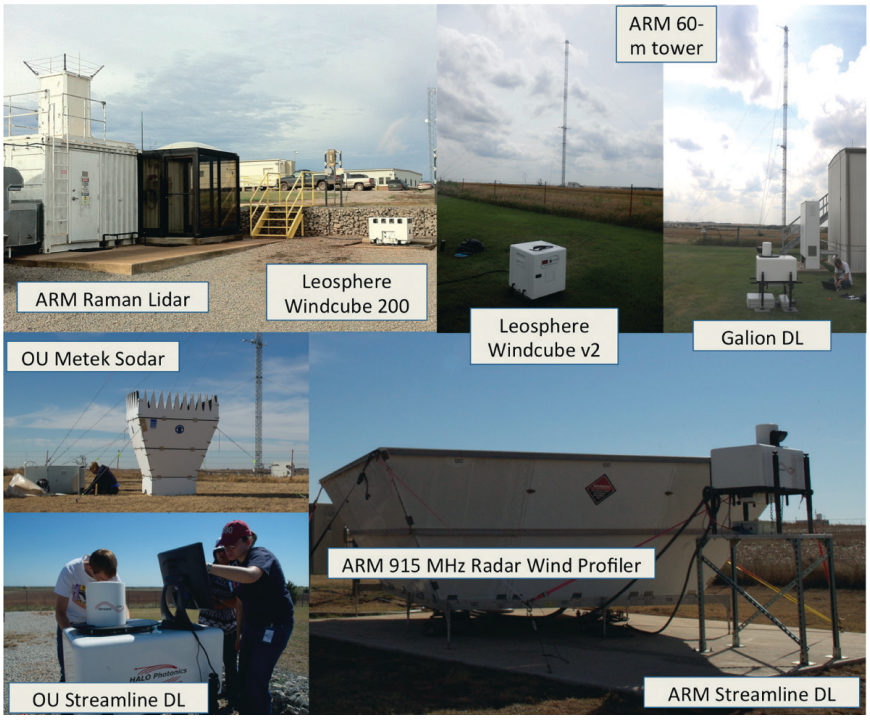

Fig. 2. Photos of the primary LABLE instrumentation deployed at the ARM SGP central facility. Details about the instrument specifications can be found in Table 1 and the location of each instrument is documented in Fig. 1. (Photos were taken by E. Jacobsen and J. Newman.)

While the scanning strategy of the WINDCUBE v2 lidar could not be changed to mitigate these issues, the scanning strategies of the three scanning lidars are entirely user defined and could be optimized for turbulence measurements. Three scanning strategies were tested during LABLE II: a tri-Doppler technique, a six-beam technique (Sathe 2012), and a virtual tower technique (Calhoun et al. 2006).

In the first strategy, the tri-Doppler technique, the beams of the three scanning lidars were pointed to approximately the same point in space to avoid the use of a scanning circle. While the ARM Streamline DL operated in its standard vertical stare mode, the OU Streamline and Galion DLs were steered toward a point 105 m above the ARM Streamline DL, which corresponds to the first useable range gate of the Streamline system. Since the radial wind speed is measured by three different lidars and there are three unknown wind components (u, v, and w), a set of three equations can be used to solve for the wind components. Although the effects of averaging within the probe volume cannot be mitigated in this way, the tri-Doppler technique allows for the measurement of turbulence within a small area of space rather than a large scanning circle and does not require the assumption of horizontal homogeneity within a scanning circle.

During LABLE II, the OU Streamline DL also evaluated a six-beam technique, which was developed by Sathe (2012) to minimize the variance contamination caused by the DBS technique. The final scanning strategy tested during LABLE II involved the use of all three scanning lidars to build a "virtual tower" over the WINDCUBE v2 lidar. This strategy was identical to the tri-Doppler technique, except the beams were moved to different heights every 10 min, forming a virtual tower with measurements at several different heights. Results from the six-beam and virtual tower measurements will be presented in separate publications that are currently in preparation.

Since one primary focus of LABLE was the comparison of turbulence parameters from different instruments, lidar quality control techniques were designed to optimize the accuracy of turbulence estimates. Two different methods were used to process the DL data and calculate variance. In the first technique, a spike filter developed by Højstrup (1993) and adapted by Vickers and Mahrt (1997) was used to remove random noise from the raw lidar velocity time series. A 10-min moving window was shifted through the raw lidar data, and any point within the window that was more than 3.5 standard deviations from the mean was flagged as a possible spike and removed from the dataset. This process was repeated until no more spikes were detected. For each iteration of the spike filter, the factor of 3.5 standard deviations was increased by 0.1 standard deviation. The variance of each velocity component was then computed by averaging the 10-min variances over a 30-min period.

The second approach used the Lenschow technique (Lenschow et al. 2000), which assumes that noise is completely random and uncorrelated. Thus, in an autocovariance plot, the noise signal should spike at lag 0, then decorrelate immediately while the true atmospheric signal shows correlation beyond lag 0 in association with coherent motions. To estimate the amount of variance that is associated with noise, the raw velocity data were first detrended to ensure that the mean was zero. Next, the autocovariance function was calculated for each velocity component. Starting from lag 1, the autocovariance function was extrapolated back to lag 0 using a slope that is derived from the inertial subrange model. The value of the extrapolated function at lag 0 was then assumed to be the true variance, while the difference between the extrapolated function and the calculated function was assumed to be the variance due to noise.

For methods other than the Lenschow technique, SNR was also used to eliminate noisy lidar data. By default, WINDCUBE v2 radial velocities that were associated with SNR < –23 dB were not recorded in the output data stream. Similarly, Streamline and Galion DL radial velocities that were associated with SNR < –21 dB were removed from the dataset. Lidars are adversely affected by the presence of precipitation particles, which can result in beam attenuation and increased vertical velocities (e.g., Huffaker and Hardesty 1996; Pearson et al. 2009). Thus, lidar data were not used when the rain gauge at the ARM site recorded precipitation.

RESULTS. In the following, some initial results from the LABLE campaign are highlighted and discussed. Since assessing the performance of the different LABLE instruments is key to the scientific objectives of the project, instrument comparisons are presented first. As expected from previous studies (Bonner 1968; Song et al. 2005), LLJs frequently developed at night during LABLE, and the discussion in the remainder of this section focuses on LLJs. After a summary of general LLJ characteristics observed during LABLE I, the dynamic, thermodynamic, and turbulence structures of the NBL during two interesting LLJ events are compared. Finally, we highlight how the finescale structure of the NBL can be resolved using different scanning strategies with multiple DLs.

Instrument comparisons. Given the multilayered structure of the NBL, it is very important to have high-resolution profiles of wind, temperature, and turbulence parameters in the layer of the atmosphere influenced by the diurnal cycle (i.e., the layer from the ground up to a height of 2–3 km). Near the surface, observations with sonic anemometers coupled with infrared gas analyzers were proven to provide reliable data of mean wind and turbulent fluxes (Foken 2008). At the ARM SGP site, the instrumented 60-m tower and the nearby ECOR system provide such measurements at 4, 25, and 60 m. The lowest reliable retrieval heights for the Streamline DLs are approximately 100 m, resulting in a data gap between 60 and 100 m that can often be filled in with observations from the sodar or the WINDCUBE v2 DL.

Sodars have been used to study the lower boundary layer since the 1970s (Coulter and Kallistratova 2004). The backscattered signal detected by sodars results from gradients in the temperature field caused by turbulent mixing (Hall et al. 1975; Anderson 2003). These structures in the temperature field are advected with the wind, so Doppler shifts in the received signals can be used to estimate properties of the wind field aloft. Doppler lidars, on the other hand, measure the Doppler shift of the backscattered energy from aerosol particles, which are assumed to be small enough to be tracers of atmospheric motion. DLs have been used in a wide range of ABL research, including studies of the CBL (e.g., Lothon et al. 2006; Träumner et al. 2011), LLJs in the nocturnal boundary layer (e.g., Banta et al. 2006), urban flow and turbulence characteristics (Newsom et al. 2008), and wakes behind wind turbines (Iungo et al. 2013; Barthelmie et al. 2014).

Given the differences in the measurement principles and possible error sources of the instruments used to construct continuous vertical ABL profiles, it is necessary to verify that their observations are

consistent with each other. Data from overlapping measurement heights were thus selected and compared to identify and quantify possible instrument errors. For these comparisons, data were used for each full day of LABLE I in which there was at least 50% data availability from the sonic anemometer at 60 m. This resulted in a dataset consisting of 24 days during the experiment. Wind speed and direction measured by the sonic anemometer are provided as 30-min averages. Data from the sodar were used if the SNR from the vertical beam was greater than 3 dB. To assure a statistically robust comparison, 10-min averages of the cluster-analyzed wind components u and υ were taken from the sodar and averaged onto the same 30-min periods as for the tower data. Wind speed and direction were then derived from the averaged u and υ values. It should be noted that the spatial average represented by the tower's sonic anemometer and the sodar are vastly different. The sonic anemometer provides a point measurement. In contrast, the sodar uses the DBS technique to derive the horizontal wind components and as such involves a spatial average across the area captured by the five beams, equating to an area of approximately 110 m^2 at 60-m height.

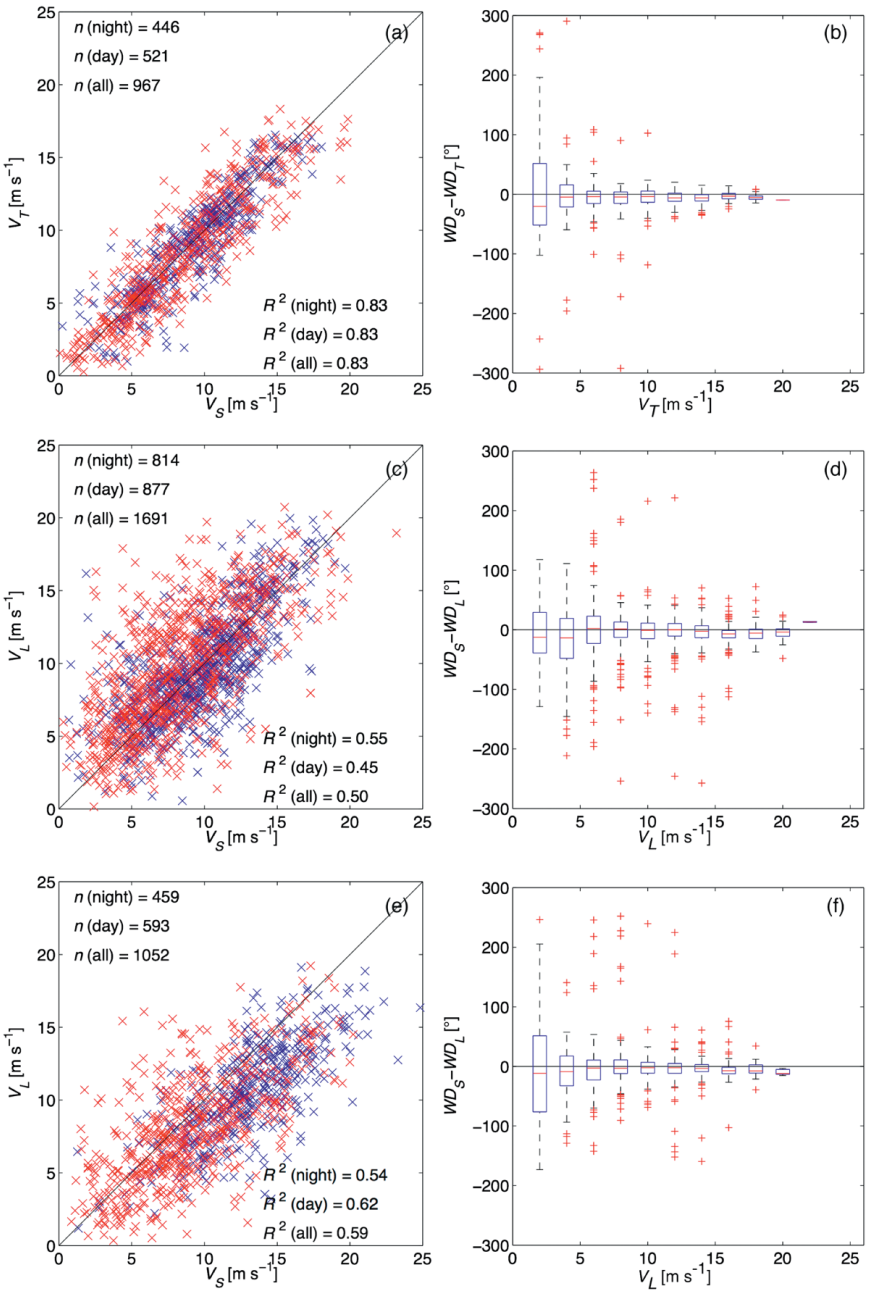

Fig. 3. Comparisons of the wind speed from (a) the sodar and the tower-mounted sonic anemometer at 60 m, (c) the sodar and OU Streamline lidar at 90 m, and (e) the sodar and the OU Streamline lidar at 160 m. The box-and-whisker plots illustrate how the differences between the wind directions measured by (b) the tower-mounted sonic anemometer and the sodar at 60 m and the sodar, and the lidar at (d) 90 and (f) 160 m decrease with increasing wind speeds. Data are grouped by day (1330–2300 UTC, red) and night (0030–1200 UTC, blue). For the wind speed comparisons, R^2 values are shown in the lower-right corner of each panel and the black line indicates the 1-to-1 line.

Figure 3a depicts a comparison of the sodar-retrieved wind speeds at 60 m to those measured with the tower-mounted sonic anemometer at 60 m. The data are separated into day and night groupings, defined as 1330–2400 and 0030–1200 UTC, respectively (local time is UTC minus 5 h). Given the spatial sampling discrepancies, the wind speeds from the two instruments agree reasonably well. Also, there are no significant

differences in the comparison statistics during the day versus at night with the R^2 values, where R is the Pearson correlation coefficient, being 0.83 for both day and night. The comparison of the wind directions (Fig. 3b), presented as a box-and-whisker plot of the differences between the wind direction measured by the sodar and sonic anemometer, grouped by wind speed, illustrates that a larger scatter in wind direction is observed for lower wind speeds, but for wind speeds $V_T > 5$ m s^{-1} (measured with the tower-mounted sonic anemometer at 60 m) the inner quartile range of the wind-direction differences is less than plus or minus 25°.

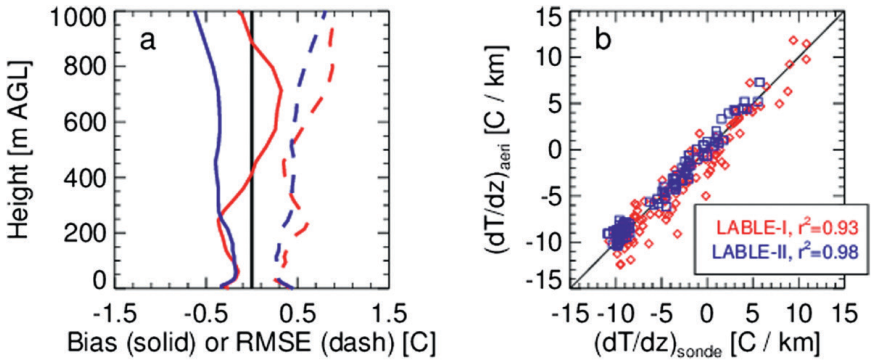

Fig. 4. (a) Mean bias (rawinsonde minus AERI) and RMSE, and (b) comparison of the temperature gradients between 10 and 100 m AGL, $dT/dz = (T_{100} - T_{10})/90$ m, determined from AERI retrievals and rawinsonde observations during LABLE I and II. The results are based on 120 (106) AERI and rawinsonde profile comparisons during LABLE I (II); see text for more details.

The same type of comparison was also conducted between the sodar and OU Streamline DL retrievals of the horizontal winds at 90 and 160 m (Figs. 3c,d and 3e,f, respectively). The winds from the OU Streamline DL were measured at an elevation angle of 70° above the horizon, and the winds from the sodar were measured at an elevation angle of 72.2°. The DL wind profiles represent a 3-min average taken at 30-min increments, while the sodar wind profiles used for this comparison represent 10-min averages taken at 30-min increments. Note that the OU Streamline DL data from a lower elevation angle (e.g., 40°) could have been compared against the sodar data, but we chose to compare data from similar elevation angles and thus similar spatial averaging volumes.

Fewer samples are available for the 160-m comparison because the maximum retrieval height of the sodar was sometimes below 160 m. Unlike the 60-m sodar–sonic anemometer comparison, the R^2 values for the lidar–sodar comparison are different at night and day, but the differences are quite small and the trends are not consistent for the two measurement heights. The scatter in the lidar-versus-sodar wind speed comparison for both wind speed and wind direction is higher than in the tower-versus-sodar comparison but a clear bias of one instrument versus the other could not be identified. The different averaging times for the two

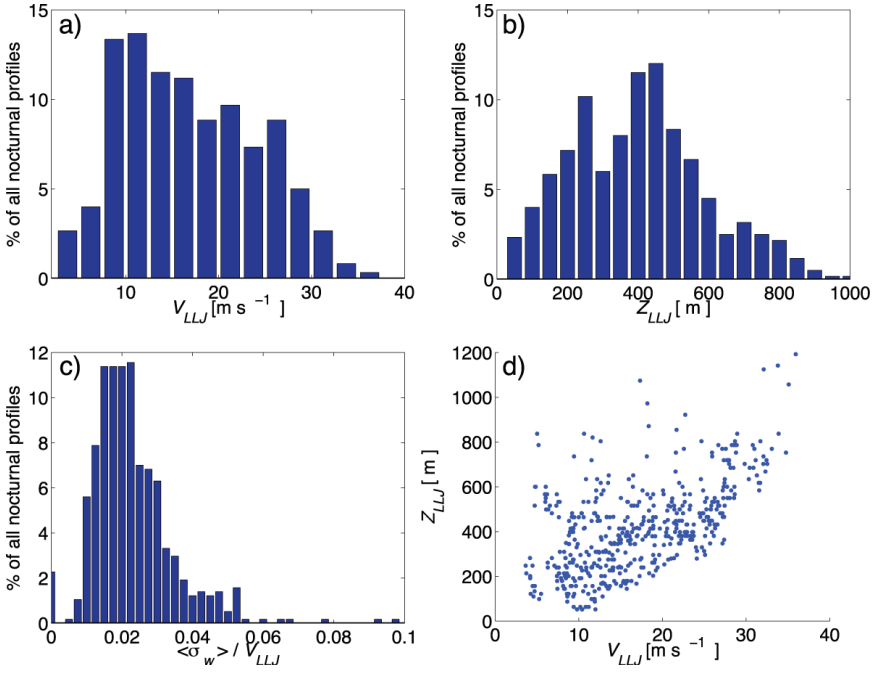

Fig. 5. Histograms of (a) the LLJ nose wind speed, (b) height of the LLJ nose, and (c) normalized mean standard deviation of the vertical velocity below the LLJ nose. (d) A scatterplot comparing the LLJ strength with the LLJ height. All statistics were computed based on a total of 599 nocturnal profiles of 30-min duration (0000–1200 UTC), for which a wind maximum within the height range of the OU Streamline DL was detected during LABLE I.

instruments will likely be one factor contributing to the higher scatter but it should also be noted that the 90-m measurement level is pushing the lower limit of reliable data for the OU Streamline DL, while 160 m is at the upper limit (or above depending on the conditions) of the sodar measurement range.

To evaluate the skill of the AERI observations in providing information about the temperature structure in the lowest 1 km of the ABL, the mean bias and root-mean-square error (RMSE) were computed by comparing temperature profiles from Atmospheric Emitted Radiance Interferometer optimal-estimation (AERIoe) retrievals (Turner and Löhnert 2014) with rawinsonde temperature profiles. The rawinsonde data were interpolated to the AERI grid heights; the current retrieval is configured to have 26 levels in the lowest 1000 m (the grid goes from 10-m resolution at the surface to 100-m resolution at 1 km). The analysis was separated into LABLE I and II, as different AERI systems were used for the two periods. In LABLE I, we applied the AERIoe retrieval to the operational AERI system, which is collecting spectral data at 30-s resolution. However, this instrument was not operating properly during LABLE II; thus, we applied the retrieval algorithm to the older AERI-01 instrument, which was running at 8-min resolution. All clear-sky rawinsonde profiles from the four-times-daily releases during LABLE I and II were included in the analysis (120 profile comparisons during LABLE I and 106 during LABLE II). The bias is less than 0.4°C up to 300 m for both LABLE I and II, and the RMSE values are almost the same (Fig. 4a). Above 300 m, the bias changes slightly between the two periods, but in both experiments the absolute bias is less than 0.5°C for all heights below 1 km. Additionally, the temperature gradients between 10 and 100 m AGL, defined as $dT/dz = (T_{100} - T_{10})/90$ m, observed by the AERI and rawinsonde temperature profiles are also compared (Fig. 4b). The comparison illustrates that the AERI observations capture the near-surface temperature structure very well during both campaigns. A tendency for a low bias can be noted for LABLE I, particularly for strong stabilities at night. However, the overall good agreement between the AERI and rawinsonde observations shows that AERI observations can be used to monitor the near-surface temperature structure of the atmospheric boundary layer, which is very important for investigating the LLJ development in more detail (see also more details below). In the remainder of the paper, we use AERI along with DL observations to provide new insights into the interplay between the thermodynamic and turbulence structure in the NBL for selected cases.

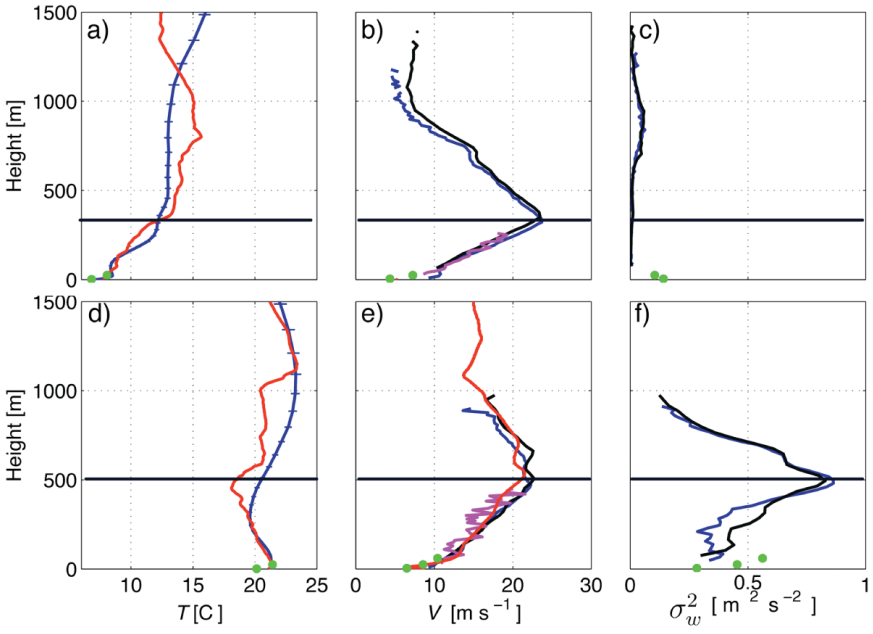

Fig. 6. Profiles of (a),(d) temperature, (b),(e) horizontal wind speed, and (c),(f) vertical velocity variance profiles at 1130 UTC (a)–(c) 9 Oct and (d)–(f) 24 Oct 2012. In (a) and (d), the blue line indicates temperatures retrieved from the AERI with associated errors, the red line is temperature observed by the rawinsonde, and the green circles show the temperature observations with the Vaisala probes on the 60-m tower and ECOR site. In (b),(c),(e), and (f), the blue line indicates values from the OU Streamline DL, the black line indicates values from the ARM Streamline DL, the magenta line indicates values from the sodar, the green circles indicate values from the sonic anemometer observations on the 60-m tower, and the red line indicates values from the rawinsonde observations (the rawinsonde wind speed data had errors on 9 Oct 2012 and are thus not shown). The black horizontal line highlights the location of the LLJ nose.

Low-level-jet development. The ARM SGP site is situated within a climatological maximum of LLJ occurrences (Bonner 1968; Song et al. 2005). During the LABLE I campaign period, LLJs with peak winds

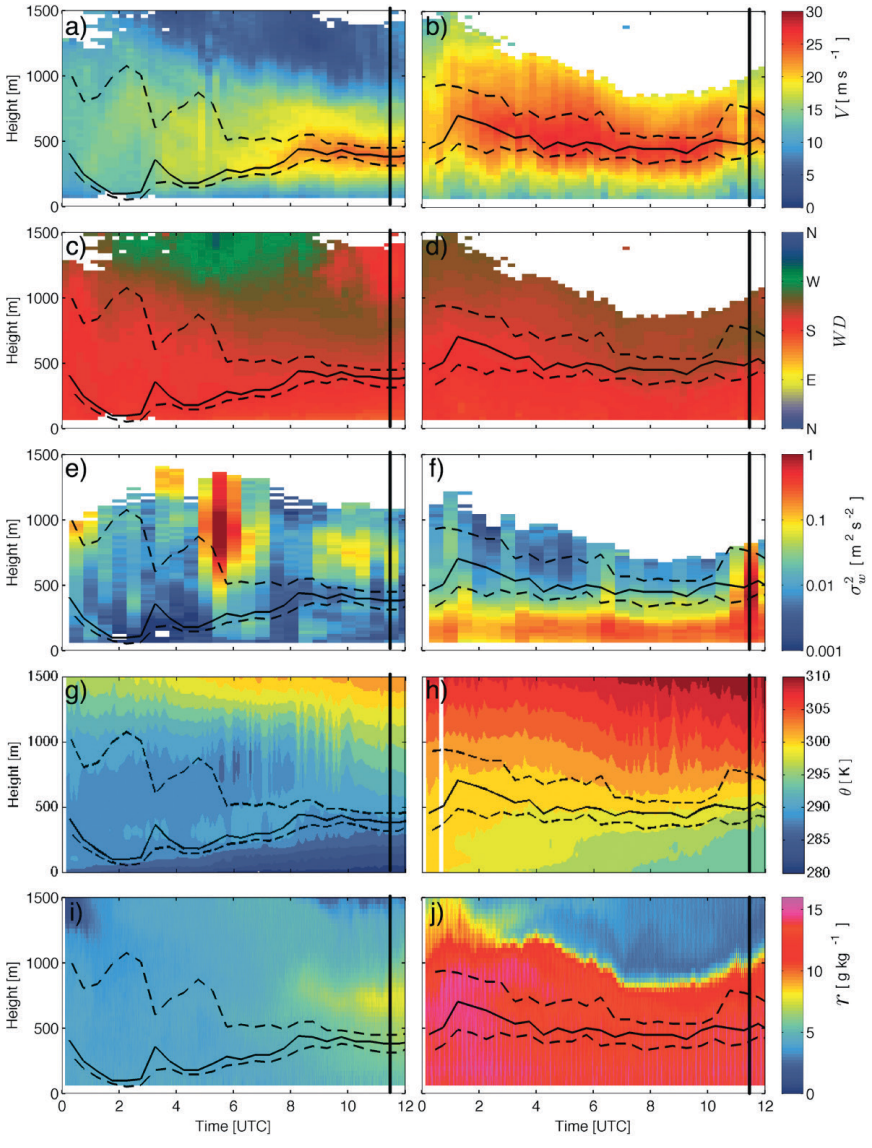

Fig. 7. Evolution of the LLJ and the associated thermodynamics on the nights of (a),(c),(e),(g),(i) 9 and (b),(d),(f),(h),(j) 24 Oct 2012 case studies. (a),(b) Shown are mean horizontal wind speed, (c),(d) wind direction, (e),(f) vertical velocity variance, (g),(h) potential temperature, and (i),(j) mixing ratio. Mean horizontal wind and direction are from VAD analyses from PPI scans with the OU Streamline DL. Vertical velocity variance is from 30 min of vertical stares from the ARM Streamline DL. Potential temperature profiles come from the AERI, and water vapor mixing ratio profiles come from the Raman lidar. The black solid line indicates the height where the LLJ nose was detected, and the dashed lines indicate the heights where the wind speed drops to 90% of the wind speed at the LLJ nose. Black vertical lines highlight the time corresponding to the profiles shown in Fig. 6.

of at least 10 m s^{-1} were observed on 20 nights. The LLJ typically developed shortly after sunset and dissipated in the early morning hours. However, the exact onset and dissipation times of the LLJ varied greatly on each individual night, often depending on synoptic conditions.

For a more detailed analysis of the LLJ evolution throughout the night, we determined the height of the LLJ nose Z_{LLJ} and the wind speed V_{LLJ} at the height of the jet nose for all nocturnal (0000–1200 UTC) wind profiles for which a wind speed maximum was detected within the height range of the OU Streamline DL during LABLE I (599 profiles in total). The determination of Z_{LLJ} and V_{LLJ} can be difficult when the nose of the LLJ (i.e., the LLJ wind speed maximum V_{max}) is not well defined. An algorithm was developed that, for all profiles with strong shear above and below the LLJ nose, assigned $V_{LLJ} = V_{max}$ and Z_{LLJ} to the height Z_{max}, where V_{max} was detected. If the shear is weak at Z_{max}, then Z_{LLJ} is assigned to the lowest height beneath V_{max} at which wind shear is less than 0.025 s^{-1}, and V_{LLJ} is the wind speed at Z_{LLJ}.

As illustrated in Fig. 5, the strength of the LLJs varied between 2.5 and 40 m s^{-1} with $V_{LLJ} \approx 10$ m s^{-1} being most frequently observed (Fig. 5a). The distribution for Z_{LLJ} shows two peaks: around 250 and 400–450 m (Fig. 5b). The heights and strengths of the LLJ appear to be correlated with stronger jets having a tendency to be deeper (Fig. 5d). However, there is significant scatter and we plan to investigate in more detail the factors that contribute to this scatter utilizing the information from the AERI temperature profiles. An important objective of LABLE was the investigation of the turbulence regimes associated with LLJs. The standard deviation of the vertical velocity σ_w can be considered an important characteristic for the intensity of vertical mixing in the

NBL. The normalized mean ratios σ_w/V_{LLJ} below the LLJ nose peaked at around 0.02 but the values ranged from 0 to 0.1 (Fig. 5c). This large range in the normalized standard deviations of vertical velocity indicates that the turbulence structure can be very different for LLJs of comparable strength.

To highlight which factors may contribute to the differences in the NBL structure during LLJ events, we selected two interesting events, which are compared in Figs. 6–8. The two LLJ cases discussed here occurred on the mornings of 9 and 24 October 2012. In each instance, the LLJ was associated with an 850-hPa low pressure area to the northwest of the ARM SGP site. Both jets were of similar magnitude, with peak nocturnal winds recorded by the OU Streamline DL of approximately 24 m s^{-1} on 9 October and 27 m s^{-1} on 24 October. Figure 6 shows temperature, wind, and vertical velocity variance profiles observed at around 1130 UTC when rawinsonde observations were made during both nights. The profile comparisons demonstrate that the DL and sodar observations agree well with the rawinsonde profiles and sonic anemometer observations. Close to the ground, the AERI observations also agree well with the rawinsonde profiles, but at the height of the LLJ nose differences on the order of 2°C can be noted, which could be significant for assessing the bulk stability of the layer below the LLJ nose (see next paragraph). On the other hand, the distinct differences in the thermodynamic boundary layer structure during both nights are well captured by the AERI. Figure 6 illustrates that while the LLJ kinematics are quite similar at this hour during both nights the thermodynamic and turbulence structures for the two LLJ events had

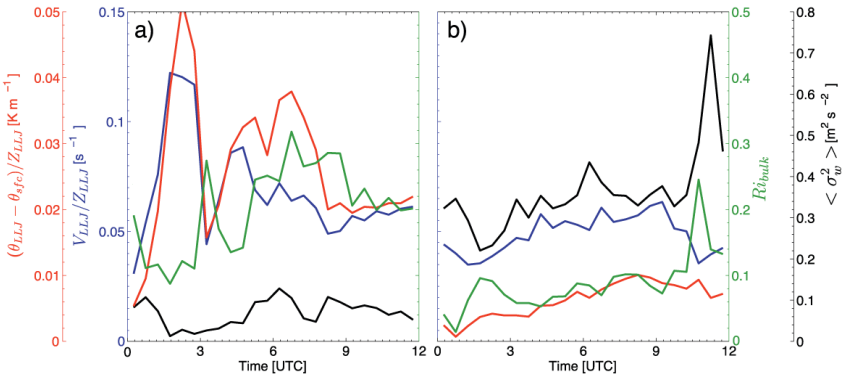

Fig. 8. Bulk shear (blue), potential temperature gradient across the layer from the surface to the LLJ nose (red), bulk Richardson number (green), and mean vertical velocity variance below the LLJ nose (black) for the nights of (a) 9 and (b) 24 Oct 2012. Shear was calculated as V_{LLJ}/Z_{LLJ}, assuming the wind speed at the surface to be 0 m s^{-1}.

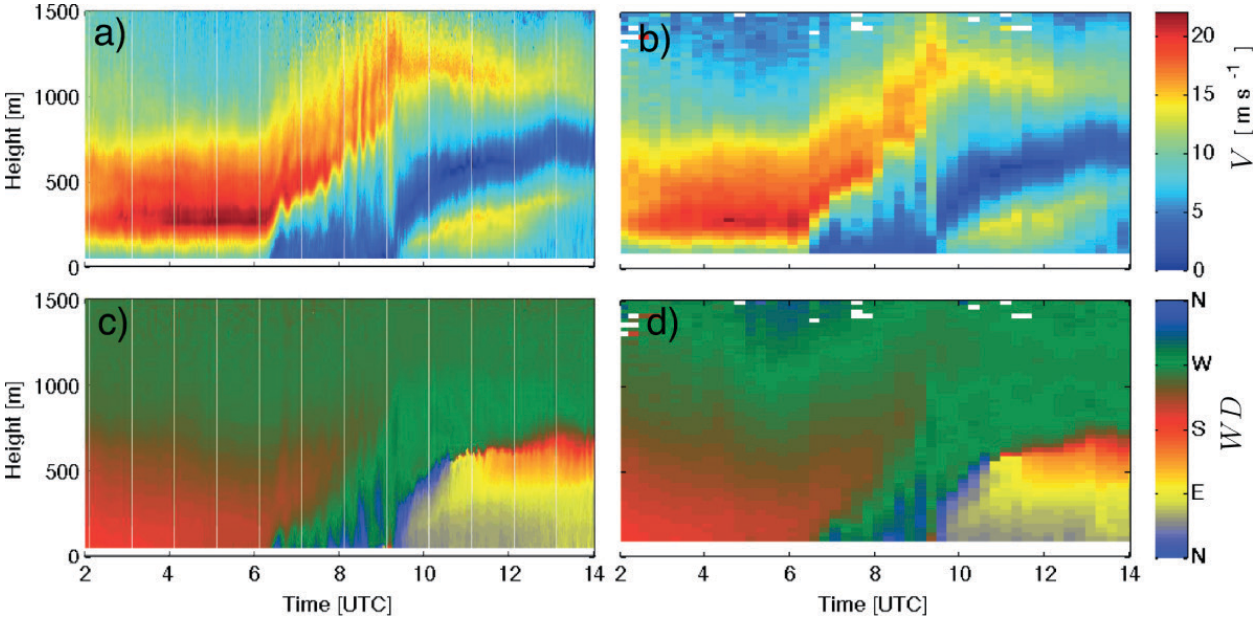

Fig. 9. (a),(b) Mean horizontal wind speeds and (c),(d) wind directions measured during LABLE II on 13 Jun 2013. Results from (a),(c) the dual-Doppler analysis with the OU Streamline and Galion DL are compared against (b),(d) the VAD profile measurements with the ARM Streamline DL.

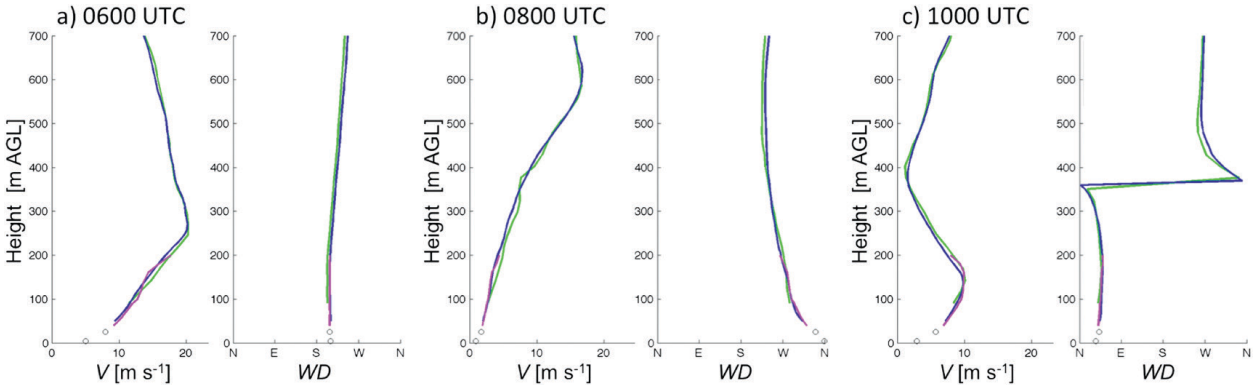

Fig. 10. Comparison of vertical profiles of mean horizontal wind speeds and wind directions measured during LABLE II at (a) 0600, (b) 0800, and (c) 1000 UTC 13 Jun 2013. Shown are results from the dual-Doppler analysis with the OU Streamline and Galion DL (blue), VAD profile measurements with the ARM Streamline DL (green), data from the LLNL Leosphere WINDCUBE v2 (pink), and the tower-mounted sonic anemometers (circles).

distinct differences. On 24 October the LLJ is associated with strong vertical mixing (Fig. 6f) and a very weak inversion near the surface (Fig. 6d); on 9 October a strong surface-based inversion developed (Fig. 6a) and turbulent mixing below the nose of the LLJ is absent (Fig. 6c), but gravity waves with strong rising–sinking motion couplets intermittently contributed to high σ^2_w values above 400 m at around 0500–0700 UTC (Fig. 7e). During both nights, the DLs reported lower σ^2_w values than did the sonic anemometers (Figs. 6c,f), which may be due to the larger probe volume of the DLs, but the different height ranges of the DLs and sonic anemometers prevent a direct, more detailed comparison.

Differences can also be noted in the onset of the LLJ development; while the LLJ developed quickly and remained relatively constant in magnitude after sunset on 24 October as the 850-hPa trough remained nearly stationary, the LLJ on 9 October developed more slowly as the winds increased overnight with the approach of the 850-hPa trough (Figs. 7a,b). Winds generally veered with height in the LLJ on both cases, and the winds became more westerly over time (Figs. 7c,d). While both LLJ events were of similar magnitude at their peaks, the LLJ on 24 October produced much stronger turbulent vertical mixing below the jet nose than the 9 October LLJ (Figs. 7e,f). In fact, significant mixing was maintained and increased over the entire night of 24 October (Fig. 8). It appears that because of the early onset of the LLJ (before a strong nocturnal inversion formed) turbulent mixing prevailed even after sunset, which prevented a strong surface-based inversion to form. Using the bulk shear (V_{LLJ}/Z_{LLJ}) computed from the DL wind profiles and potential temperature gradient across the layer from the surface to the LLJ nose [$(\theta_{LLJ} - \theta_{sfc})/Z_{LLJ}$] determined from the AERI temperature profiles, a bulk Richardson number Ri_{bulk} was computed according to

$$\mathrm{Ri}_{bulk} = \frac{g}{\theta}\frac{(\theta_{LLJ} - \theta_{sfc})/Z_{LLJ}}{(V_{LLJ}/Z_{LLJ})^2}, \quad (1)$$

where g is the gravitational acceleration and θ is the mean potential temperature in the layer from the surface to the height Z_{LLJ}. On 24 October, Ri_{bulk} remained below 0.1 almost throughout the entire night (Fig. 8b), further confirming that the layer below the LLJ nose was only weakly stable. In contrast, the LLJ developed much later on 9 October. Mechanical generation of turbulence below the LLJ nose was thus very weak or nearly absent at sunset and a strong surface-based inversion formed quickly after sunset, with Ri_{bulk} reaching values as high as 0.25–0.3 (Figs. 7g,h and 8a), which corresponds to the Ri_{bulk} threshold identified in previous studies for the transition to very stable boundary layers where turbulence becomes intermittent (Banta et al. 2003; Mahrt 1999). As mentioned above, uncertainties in the AERI temperature observation at Z_{LLJ} affect the accuracy of the Ri_{bulk} values, but Ri_{bulk} values computed from AERI and rawinsonde profiles at 0600 and 1200 UTC correlated very well with a slope of 0.91 for the AERI relative to the rawinsonde Ri_{bulk} values. Individual values such as the spike around 1100 UTC October 24 (Fig. 8b) might be questionable (Ri_{bulk} computed using temperature data from the rawinsonde at 1200 UTC was 0.09), but the overall trends are well captured by the AERI data and it is clear that the atmospheric stability below the LLJ was very different during the two episodes. With the inversion in place by the time winds increased to greater than 20 m s^{-1}, the strong static stability suppressed any mechanical generation of turbulence by the LLJ. Consequently, with less mixing, it is plausible that the LLJ was narrower and shear below the LLJ nose was stronger in the 9 October case compared with the 24 October

LLJ (Figs. 7 and 8). The water vapor mixing ratio (r) data from the Raman lidar observations (Figs. 7i,j) show that the LLJ on 24 October was associated with much higher atmospheric humidity throughout approximately the lowest 1 km than on 9 October.

High-resolution lidar observations. As discussed in the previous sections, horizontal wind speed can be accurately measured with DLs. However, the temporal resolution is reduced as a result of the time it takes to perform a PPI scan, and it is difficult to obtain accurate turbulence statistics from PPI scans. During LABLE II we used a tri-Doppler technique that provides all three velocity components at 1-s temporal resolution. We used these measurements to construct 30-s-averaged wind profiles, which were compared against traditional VAD analysis profiles that were collected every 30 min by the ARM Streamline DL (Figs. 9 and 10) for 13 June 2013 when a strong LLJ developed that was lifted by the passage of a frontal boundary. The general LLJ evolution and its interaction with the mesoscale frontal boundary are well captured by the single DL VAD measurements (Figs. 9b,d), but only the high-resolution observations with the two horizontally staring DLs (Figs. 9a,c) capture the high-frequency oscillations in the wind field that developed as the LLJ was lifted by the front.

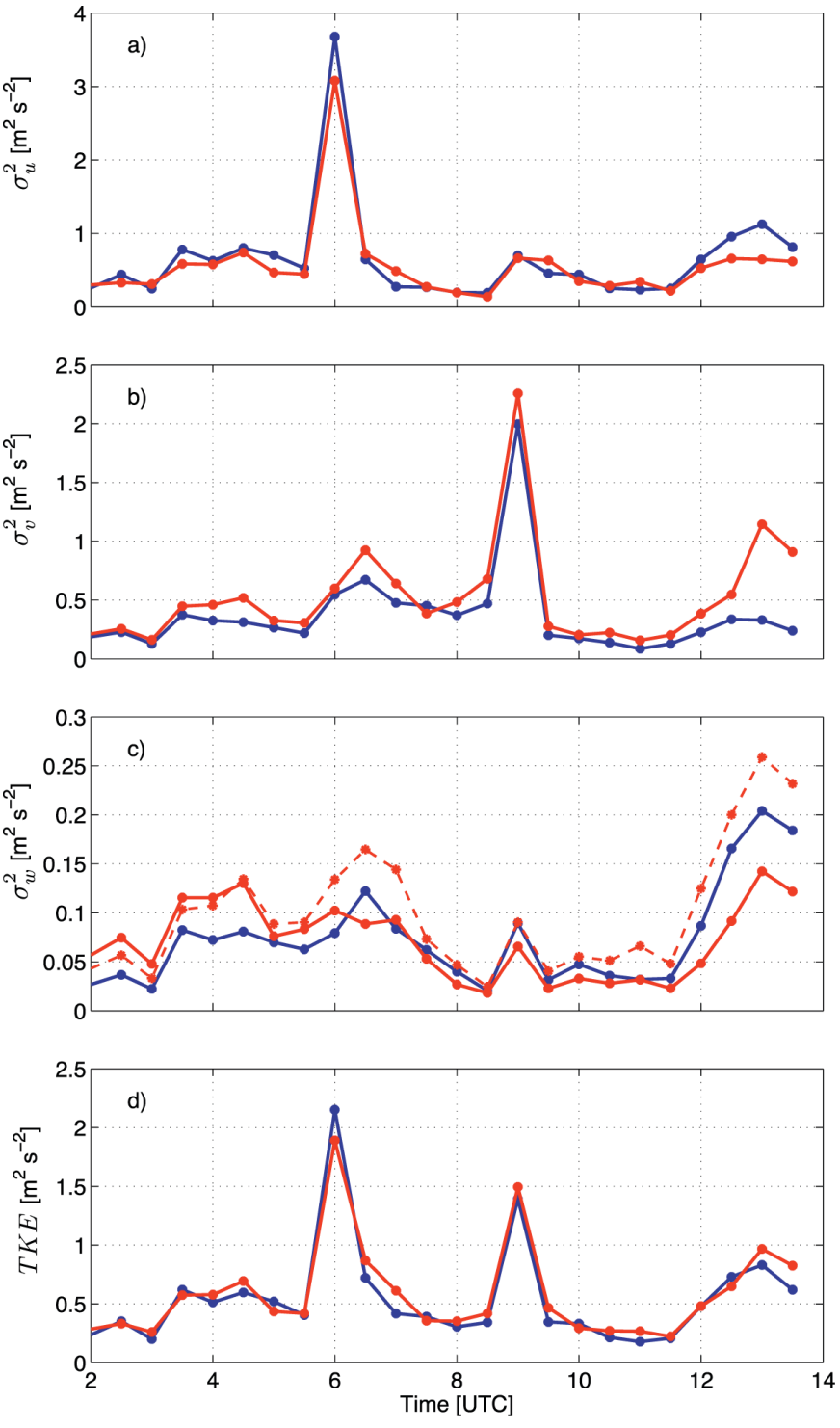

Fig. 11. Comparison of 30-min variances of (a) u, (b) v, and (c) w, and (d) TKE measured during LABLE II on 13 Jun 2013 at a height of 105 m AGL. Shown are results from the tri-Doppler analysis with the ARM Streamline, OU Streamline, and Galion lidar (blue) and data from the LLNL Leosphere WINDCUBE v2 (red). The dashed red line in (c) shows the results of the vertical velocity variance retrieved from the vertical beam measurements of the LLNL Leosphere WINDCUBE v2. See text for more details about the different lidar scans and related analysis routines.

The reconstructions of the wind profiles from the two horizontal lidar stares (dual-Doppler analysis) require that measurements from different range gates from the two DLs be combined (the lidar beams intersect perfectly only at z = 105 m AGL but will be focused at different x and y coordinates for the other heights), which could potentially lead to discrepancies in the wind profiles. As shown in Fig. 10, the dual-Doppler mean wind profiles compare very well with the VAD profile measurements from both the ARM Streamline DL and the Leosphere WINDCUBE v2.

The high-resolution measurements were then also used to evaluate the Leosphere WINDCUBE v2 measurements of turbulence statistics. Time series of 30-min-averaged velocity variances σ^2_u, σ^2_v, and σ^2_w, and turbulence kinetic energy (TKE) from 13 June 2013 are shown in Fig. 11. While the TKE measurements from the Leosphere WINDCUBE v2 generally agree well with the tri-Doppler data, some differences can be noted in the individual velocity variances. The WINDCUBE values for σ^2_v are consistently higher than the tri-Doppler data, which indicates that variance contamination by cross components of the Reynolds stress tensor (Sathe and Mann 2012) affects the WINDCUBE v2 measurements. However, the results for σ^2_u and σ^2_w show less-clear trends and further investigations are necessary to determine what causes the both higher and lower values of the WINDCUBE v2 variances compared to the tri-Doppler results. The accuracy of velocity variance and TKE measurements with different DL scanning techniques is currently further evaluated using turbulence parameters computed from 60-Hz sonic time series collected during the Lower Atmospheric Thermodynamics and Turbulence Experiment (LATTE) at the Boulder Atmospheric Observatory in early 2014. During LATTE, sonic anemometers were deployed at six levels from 50 to 300 m AGL—an ideal range for the comparison with DL observations.

SUMMARY AND FUTURE WORK. Leveraging ongoing collaborations between researchers and instrumentation from various agencies, the OU BLISS group was able to deploy multiple DLs and a sodar during two campaigns at the ARM SGP site. Graduate students played a leading role in the design of the experiments, the deployment and operation of the instruments, and the scientific data analysis. The sodar and DL measurements were combined with measurements from existing instrumentation at the ARM site to create rich datasets, which capture the dynamic, thermodynamic, and turbulence structures of the ABL for a wide range of synoptic conditions.

Our results indicate generally good agreement between mean wind speeds and directions measured by the various instruments during the campaign, which allows us to aggregate data from different instruments into profiles that capture the dynamic ABL structure in the lowest 2–3 km at high resolution. Having wind, turbulence, and temperature (from the AERI) profiles at high temporal resolution is a unique aspect of the LABLE datasets and we are not aware of other studies that measured the dynamic, turbulence, and thermodynamic ABL structures below 1 km at similar resolution for extended time periods. We demonstrated that the AERI observations accurately capture the near-surface temperature gradients; that is, the thermodynamic structure of the surface layer can be studied at high temporal resolution. As shown in the analysis of several LLJ cases, such datasets can provide new insights into the interplay between the dynamic, thermodynamic, and turbulence structures in the NBL. The time of LLJ onset appears to play a critical role in the decay or persistence of turbulent mixing after sunset. We presented a summary of general LLJ characteristics and discussed interesting features of individual LLJ cases. A more in-depth analysis that focuses on correlations between LLJ and stability parameters was conducted by one of the graduate students as part of his Ph.D. research (Bonin 2015; Bonin et al. 2015). Also, the skill of DLs in measuring turbulence statistics using different scanning strategies was evaluated more systematically by another graduate student as part of her Ph.D. thesis (Newman 2015). The LABLE campaigns thus provided valuable datasets for multiple student projects, and we expect several additional journal articles to be published in the near future. Work is also under way to quantify the water vapor flux at the top of the CBL over a range of conditions, and the datasets are also used to study the spatial and temporal variability of turbulence and how this variability is linked to land use near the ARM site. Future work will also focus on additional case studies of cold fronts and gravity waves, incorporating data from ARM's K-, X-, and C-band radars, which provide valuable scans over the site to potentially complement observations made by the other instruments mentioned in this paper. The LABLE DL and sodar observations, as well as AERIoe retrievals, are available in the ARM archive.

ACKNOWLEDGMENTS. This research was supported by NOAA's National Severe Storms Laboratory and the Department of Energy's (DOE) Atmospheric System Research (ASR, Grant DE-SC0006898) program. The OU lidar was purchased using funds from the NSF Career

Award ILREUM (NSF ATM 0547882) and the Office of the Vice President for Research at the University of Oklahoma. The OU sodar was purchased using funds from the NSF (NSF AGS 1229181). The rental of the Galion DL and the loan of the WINDCUBE v2 were provided by a grant with Lawrence Livermore National Laboratory (Project 130180). These grants also provided funding for the majority of the authors. In addition, SW was funded by an LLNL Laboratory Directed Research and Development (LDRD) grant (12-ERD-069). We thank Matthieu Boquet, Mehdi Machta, and the rest of the Leosphere team for generously loaning their lidar to us for this project and for their support during and after the experiment. We are also grateful for the support of the SGURR Energy team around Gareth Brown and Nick Capaldo in the setup of the Galion DL and data processing. The ARM data used in this paper were collected by the DOE Atmospheric Radiation Measurement (ARM) program and are available via its data archive (www.archive.arm.gov). We would also like to thank the ARM SGP staff for their support during the campaign.

REFERENCES

Acevedo, O. C., and D. R. Fitzjarrald, 2001: The early evening surface-layer transition: Temporal and spatial variability. *J. Atmos. Sci.,* **58,** 2650–2667, doi:10.1175/1520-0469(2001)058<2650:TEESLT>2.0.CO;2.

Anderson, P. S., 2003: Fine-scale structure observed in a stable atmospheric boundary layer by sodar and kite-borne tethersonde. *Bound.-Layer Meteor.,* **107,** 323–351, doi:10.1023/A:1022171009297.

Baas, P., F. C. Bosveld, H. Klein Baltink, and A. A. M. Holtslag, 2009: A climatology of nocturnal low-level jet at Cabauw. *J. Appl. Meteor. Climatol.,* **48,** 1627–1642, doi:10.1175/2009JAMC1965.1.

Baklanov, A. A., and Coauthors, 2011: The nature, theory, and modeling of atmospheric planetary boundary layers. *Bull. Amer. Meteor. Soc.,* **92,** 123–128, doi:10.1175/2010BAMS2797.1.

Banta, R. M., 2008: Stable-boundary-layer regimes from the perspective of the low-level jet. *Acta Geophys.,* **56,** 58–87, doi:10.2478/s11600-007-0049-8.

——, R. K. Newsom, J. K. Lundquist, Y. L. Pichugina, R. L. Coulter, and L. Mahrt, 2002: Nocturnal low-level jet characteristics over Kansas during CASES-99. *Bound.-Layer Meteor.,* **105,** 221–252, doi:10.1023/A:1019992330866.

——, Y. L. Pichugina, and R. K. Newsom, 2003: Relationship between low-level jet properties and turbulence kinetic energy in the nocturnal stable boundary layer. *J. Atmos. Sci.,* **60,** 2549–2555, doi:10.1175/1520-0469(2003)060<2549:RBLJPA>2.0.CO;2.

——, ——, and W. A. Brewer, 2006: Turbulent velocity-variance profiles in the stable boundary layer generated by a nocturnal low-level jet. *J. Atmos. Sci.,* **63,** 2700–2719, doi:10.1175/JAS3776.1.

——, ——, N. D. Kelley, R. M. Hardesty, and W. A. Brewer, 2013: Wind energy meteorology: Insight into wind properties in the turbine-rotor layer of the atmosphere from high-resolution Doppler lidar. *Bull. Amer. Meteor. Soc.,* **94,** 883–902, doi:10.1175/BAMS-D-11-00057.1.

Barthelmie, R. J., and Coauthors, 2014: 3D wind and turbulence characteristics of the atmospheric boundary layer. *Bull. Amer. Meteor. Soc.,* **95,** 743–756, doi:10.1175/BAMS-D-12-00111.1.

Beyrich, F., D. Kalass, and U. Weisensee, 1997: Influence of the nocturnal low-level jet on the vertical and mesoscale structure of the stable boundary layer as revealed from Doppler-sodar-observations. *Acoustic Remote Sensing Applications,* S. P. Singal, Ed., Narosa Publishing, 236–246.

Blackadar, A. K., 1957: Boundary layer wind maxima and their significance for the growth of nocturnal inversions. *Bull. Amer. Meteor. Soc.,* **38,** 283–290.

Bonin, T. A., 2015: Nocturnal boundary layer and low-level jet characteristics under different turbulence regimes. Ph.D. dissertation, University of Oklahoma, 169 pp.

——, W. G. Blumberg, P. M. Klein, and P. B. Chilson, 2015. Thermodynamic and turbulence characteristics of the southern Great Plains nocturnal boundary layer under differing turbulent regimes. *Bound.-Layer Meteor.,* in press.

Bonner, W. D., 1968: Climatology of the low level jet. *Mon. Wea. Rev.,* **96,** 833–850, doi:10.1175/1520-0493(1968)096<0833:COTLLJ>2.0.CO;2.

Brook, R. R., 1985: The Koorin nocturnal low-level jet. *Bound.-Layer Meteor.,* **32,** 133–154, doi:10.1007/BF00120932.

Calhoun, R., R. Heap, M. Princevac, R. Newsom, H. Fernando, and D. Ligon, 2006: Virtual towers using coherent Doppler lidar during the Joint Urban 2003 dispersion experiment. *J. Appl. Meteor. Climatol.,* **45,** 1116–1126, doi:10.1175/JAM2391.1.

Cariou, J.-P., 2011: Pulsed lidars. *Remote Sensing for Wind Energy,* A. Peña and C. B. Hasager, Eds., Risø Rep. Risø-I-3184(EN), 65–81.

Comstock, J. M., and Coauthors, 2007: An intercomparison of microphysical retrieval for upper-tropospheric ice clouds. *Bull. Amer. Meteor. Soc.,* **88,** 191–204, doi:10.1175/BAMS-88-2-191.

Cook, D. R., 2011: Eddy correlation flux measurement system handbook. Department of Energy Rep. DOE/SC-ARM/TR-052, 16 pp. [Available online at www.arm.gov/publications/tech_reports/handbooks/ecor_handbook.pdf?id=73.]

Coulter, R. L., and M. A. Kallistratova, 2004: Two decades of progress in SODAR techniques: A review of 11 ISARS proceedings. *Meteor. Atmos. Phys.,* **85,** 3–19, doi:10.1007/s00703-003-0030-2.

Feltz, W. F., W. L. Smith, R. O. Knuteson, H. E. Revercomb, H. M. Woolf, and H. B. Howell, 1998: Meteorological applications of temperature and water vapor retrievals from the ground-based Atmospheric Emitted Radiance Interferometer (AERI). *J. Appl. Meteor.,* **37,** 857–875, doi:10.1175/1520-0450(1998)037<0857:MAOTAW>2.0.CO;2.

——, ——, H. B. Howell, R. O. Knuteson, H. Woolf, and H. E. Revercomb, 2003: Near-continuous profiling of temperature, moisture, and atmospheric stability using the Atmospheric Emitted Radiance Interferometer (AERI). *J. Appl. Meteor.,* **42,** 584–597, doi:10.1175/1520-0450(2003)042<0584:NPOTMA>2.0.CO;2.

Fernando, H. J. S., and J. C. Weil, 2010: Whither the stable boundary layer? A shift in the research agenda. *Bull. Amer. Meteor. Soc.,* **91,** 1475–1484, doi:10.1175/2010BAMS2770.1.

Ferrare, R. A., and Coauthors, 2006: Evaluation of daytime measurements of aerosols and water vapor made by an operational Raman lidar over the southern Great Plains. *J. Geophys. Res.,* **111,** D05S08, doi:10.1029/2005JD005836.

Fischer, M. L., 2004: Carbon Dioxide Flux Measurement Systems (CO_2FLX) handbook. Department of Energy Rep. DOE/SC-ARM/TR-048, 12 pp. [Available online at www.arm.gov/publications/tech_reports/handbooks/co2flx_handbook.pdf?id=44.]

Foken, T., 2008: *Micrometeorology.* Springer, 299 pp.

Friedrich, K., J. K. Lundquist, M. Aitken, E. A. Kalina, and R. F. Marshall, 2012: Stability and turbulence in the atmospheric boundary layer: A comparison of remote sensing and tower observations. *Geophys. Res. Lett.,* **39,** L03801, doi:10.1029/2011GL050413.

Gero, P. J., and D. D. Turner, 2011: Long-term trends in downwelling spectral infrared radiance over the U.S. southern Great Plains. *J. Climate,* **24,** 4831–4843, doi:10.1175/2011JCLI4210.1.

Goldsmith, J. E. M., F. H. Blair, S. E. Bisson, and D. D. Turner, 1998: Turn-key Raman lidar for profiling water vapor, clouds, and aerosols. *Appl. Opt.,* **37,** 4979–4990, doi:10.1364/AO.37.004979.

Hall, F. F., Jr., J. G. Edinger, and W. D. Neff, 1975: Convective plumes in the planetary boundary layer, investigated with an acoustic echo sounder. *J. Appl. Meteor.,* **14,** 513–523, doi:10.1175/1520-0450(1975)014<0513:CPITPB>2.0.CO;2.

Hoecker, W. H., 1963: Three southerly low-level jet systems delineated by the Weather Bureau special pibal network of 1961. *Mon. Wea. Rev.,* **91,** 573–582, doi:10.1175/1520-0493(1963)091<0573:TSLJSD>2.3.CO;2.

Højstrup, J., 1993: A statistical data screening procedure. *Meas. Sci. Technol.,* **4,** 153–157, doi:10.1088/0957-0233/4/2/003.

Holtslag, A. A. M., and Coauthors, 2013: Stable atmospheric boundary layers and diurnal cycles: Challenges for weather and climate models. *Bull. Amer. Meteor. Soc.,* **94,** 1691–1706, doi:10.1175/BAMS-D-11-00187.1.

Hu, X.-M., P. Klein, and M. Xue, 2013a: Evaluation of the updated YSU planetary boundary layer scheme within WRF for wind resource and air quality assessments. *J. Geophys. Res. Atmos.,* **118,** 10 490–10 505, doi:10.1002/jgrd.50823.

——, ——, ——, J. K. Lundquist, F. Zhang, and Y. Qi, 2013b: Impact of low-level jets on the nocturnal urban heat island intensity in Oklahoma City. *J. Appl. Meteor. Climatol.,* **52,** 1779–1802, doi:10.1175/JAMC-D-12-0256.1.

——, ——, ——, F. Zhang, D. Doughty, and J. Fuentes, 2013c: Impact of the vertical mixing induced by low-level jets on boundary layer ozone concentration. *Atmos. Environ.,* **70,** 123–130, doi:10.1016/j.atmosenv.2012.12.046.

Huffaker, R. M., and R. M. Hardesty, 1996: Remote sensing of atmospheric wind velocities using solid-state and CO_2 coherent laser systems. *Proc. IEEE,* **84,** 181–204, doi:10.1109/5.482228.

Iungo, G. V., Y.-T. Wu, and F. Porté-Agel, 2013: Field measurements of wind turbine wakes with lidars. *J. Atmos. Oceanic Technol.,* **30,** 274–287, doi:10.1175/JTECH-D-12-00051.1.

Kaimal, J. C., and J. J. Finnigan, 1994: *Atmospheric Boundary Layer Flows: Their Structure and Measurement.* Oxford University Press, 304 pp.

Klein, P. M., X.-M. Hu, and M. Xue, 2014: Impacts of mixing processes in the nocturnal atmospheric boundary layer on urban ozone concentrations. *Bound.-Layer Meteor.,* **150,** 107–130, doi:10.1007/s10546-013-9864-4.

Knuteson, R. O., and Coauthors, 2004a: The Atmospheric Emitted Radiance Interferometer (AERI). Part I: Instrument design. *J. Atmos. Oceanic Technol.,* **21,** 1763–1776, doi:10.1175/JTECH-1662.1.

——, and Coauthors, 2004b: The Atmospheric Emitted Radiance Interferometer (AERI). Part II: Instrument performance. *J. Atmos. Oceanic Technol.,* **21,** 1777–1789, doi:10.1175/JTECH-1663.1.

Lenschow, D. H., V. Wulfmeyer, and C. Senff, 2000: Measuring second- through fourth-order moments in noisy data. *J. Atmos. Oceanic Technol.,* **17,** 1330–1347, doi:10.1175/1520-0426(2000)017<1330:MSTFOM>2.0.CO;2.

Lothon, M., D. H. Lenschow, and S. D. Mayor, 2006: Coherence and scale of vertical velocity in the convective boundary layer from a Doppler lidar. *Bound.-Layer Meteor.,* **121,** 521–536, doi:10.1007/s10546-006-9077-1.

Mace, G. G., T. P. Ackerman, P. Minnis, and D. F. Young, 1998: Cirrus layer microphysical properties derived from surface-based millimeter radar and infrared interferometer data. *J. Geophys. Res.,* **103,** 23 207–23 216, doi:10.1029/98JD02117.

Mahrt, L., 1999: Stratified atmospheric boundary layers. *Bound.-Layer Meteor.,* **90,** 375–396, doi:10.1023/A:1001765727956.

——, 2014: Stably stratified atmospheric boundary layers. *Annu. Rev. Fluid Mech.,* **46,** 23–45, doi:10.1146/annurev-fluid-010313-141354.

Mather, J. H., and J. W. Voyles, 2013: The ARM Climate Research Facility: A review of structure and capabilities. *Bull. Amer. Meteor. Soc.,* **94,** 377–392, doi:10.1175/BAMS-D-11-00218.1.

Mitchell, M. K., R. W. Arritt, and K. Labas, 1995: An hourly climatology of the summertime Great Plains low-level jet using wind profiler observations. *Wea. Forecasting,* **10,** 576–591, doi:10.1175/1520-0434(1995)010<0576:ACOTWS>2.0.CO;2.

Mlawer, E. J., V. H. Payne, J.-L. Moncet, J. S. Delamere, M. J. Alvarado, and D. C. Tobin, 2012: Development and recent evaluation of the MT_CKD model of continuum absorption. *Philos. Trans. Roy. Meteor. Soc.,* **370A,** 2520–2556, doi:10.1098/rsta.2011.0295.

Newman, J. F., 2015: Optimizing lidar scanning strategies for wind energy turbulence measurements. Ph.D. dissertation, University of Oklahoma, 212 pp.

Newsom, R. K., R. Calhoun, D. Ligon, and J. Allwine, 2008: Linearly organized turbulence structures observed over a suburban area by dual-Doppler lidar. *Bound.-Layer Meteor.,* **127,** 111–130, doi:10.1007/s10546-007-9243-0.

——, D. D. Turner, B. Mielke, M. Clayton, R. A. Ferrare, and C. Sivaraman, 2009: The use of simultaneous analog and photon counting detection for Raman lidar. *Appl. Opt.,* **48,** 3903–3914, doi:10.1364/AO.48.003903.

——, ——, and J. E. M. Goldsmith, 2013: Long-term evaluation of temperature profiles measured by an operational Raman lidar. *J. Atmos. Oceanic Technol.,* **30,** 1616–1634, doi:10.1175/JTECH-D-12-00138.1.

NRC, 2009: *Observing Weather and Climate from the Ground Up: A Nationwide Network of Networks*. Committee on Developing Mesoscale Meteorological Observational Capabilities to Meet Multiple National Needs, 250 pp.

——, 2010: When Weather Matters: Science and Services to Meet Critical Societal Needs. Committee on Progress and Priorities of U.S. Weather Research and Research-to-Operations Activities, 198 pp.

Parish, T. R., A. R. Rodi, and R. D. Clark, 1988: A case study of the summertime Great Plains low level jet. *Mon. Wea. Rev.,* **116,** 94–105, doi:10.1175/1520-0493(1988)116<0094:ACSOTS>2.0.CO;2.

Pearson, G., F. Davies, and C. Collier, 2009: An analysis of the performance of the UFAM pulsed Doppler lidar for observing the boundary layer. *J. Atmos. Oceanic Technol.,* **26,** 240–250, doi:10.1175/2008JTECHA1128.1.

Sathe, A., 2012: Influence of wind conditions on wind turbine loads and measurement of turbulence using lidars. Ph.D. thesis, Delft University, 158 pp.

——, and J. Mann, 2012: Turbulence measurements using six lidar beams. *Extended Abstracts, 16th Int. Symp. for the Advancement of Boundary-Layer Remote Sensing,* Boulder, CO, NOAA–CIRES, 302–305.

——, ——, J. Gottschall, and M. S. Courtney, 2011: Can wind lidars measure turbulence? *J. Atmos. Oceanic Technol.,* **28,** 853–868, doi:10.1175/JTECH-D-10-05004.1.

Song, J., K. Liao, R. L. Coulter, and B. M. Lesht, 2005: Climatology of the low-level jet at the Southern Great Plains Atmospheric Boundary Layer Experiments site. *J. Appl. Meteor.,* **44,** 1593–1606, doi:10.1175/JAM2294.1.

Stensrud, D. J., 1996: Importance of low-level jets to climate: A review. *J. Climate,* **9,** 1698–1711, doi:10.1175/1520-0442(1996)009<1698:IOLLJT>2.0.CO;2.

Strauch, R. G., D. A. Merritt, K. P. Moran, K. B. Earnshaw, and D. V. De Kamp, 1984: The Colorado Wind-Profiling Network. *J. Atmos. Oceanic Technol.,* **1,** 37–49, doi:10.1175/1520-0426(1984)001<0037:TCWPN>2.0.CO;2.

Stull, R. B., 1988: *An Introduction to Boundary Layer Meteorology.* Springer, 684 pp.

Tobin, D. C., and Coauthors, 1999: Downwelling spectral radiance observation at the SHEBA ice station: Water vapor continuum measurements from 17 to 26 μm. *J. Geophys. Res.,* **104,** 2081–2092, doi:10.1029/1998JD200057.

Träumner, K., C. Kottmeier, U. Corsmeier, and A. Wiser, 2011: Convective boundary-layer entrainment: Short review and progress using Doppler lidar. *Bound.-Layer Meteor.,* **141,** 369–391, doi:10.1007/s10546-011-9657-6.

Turner, D. D., 2007: Improved ground-based liquid water path retrievals using a combined infrared and microwave approach. *J. Geophys. Res.,* **112,** D15204, doi:10.1029/2007JD008530.

——, 2008: Ground-based retrievals of optical depth, effective radius, and composition of airborne mineral

dust above the Sahel. *J. Geophys. Res.,* **113,** D00E03, doi:10.1029/2008JD010054.

——, and J. E. M. Goldsmith, 1999: Twenty-four-hour Raman lidar water vapor measurements during the Atmospheric Radiation Measurement program's 1996 and 1997 water vapor intensive observation periods. *J. Atmos. Oceanic Technol.,* **16,** 1062–1076, doi:10.1175/1520-0426(1999)016<1062:TFHRLW>2.0.CO;2.

——, and U. Löhnert, 2014: Information content and uncertainties in thermodynamic profiles and liquid cloud properties retrieved from the ground-based Atmospheric Emitted Radiance Interferometer (AERI). *J. Appl. Meteor. Climatol.,* **53,** 752–771, doi:10.1175/JAMC-D-13-0126.1.

——, R. A. Ferrare, L. A. Heilman Brasseur, W. F. Feltz, and T. P. Tooman, 2002: Automated retrievals of water vapor and aerosol profiles from an operational Raman lidar. *J. Atmos. Oceanic Technol.,* **19,** 37–50, doi:10.1175/1520-0426(2002)019<0037:AROWVA>2.0.CO;2.

——, and Coauthors, 2004: The QME AERI LBLRTM: A closure experiment for downwelling high spectral resolution infrared radiance. *J. Atmos. Sci.,* **61,** 2657–2675, doi:10.1175/JAS3300.1.

——, V. Wulfmeyer, L. K. Berg, and J. H. Schween, 2014: Water vapor turbulence profiles in stationary continental convective mixed layers. *J. Geophys. Res. Atmos.,* **119,** 11 151–11 165, doi:10.1002/2014JD022202.

Vickers, D., and L. Mahrt, 1997: Quality control and flux sampling problems for tower and aircraft data. *J. Atmos. Oceanic Technol.,* **14,** 512–526, doi:10.1175/1520-0426(1997)014<0512:QCAFSP>2.0.CO;2.

Walters, C. K., J. A. Winkler, R. P. Shadbolt, J. van Ravensway, and G. D. Bierly, 2008: A long-term climatology of southerly and northerly low-level jets for the central United States. *Ann. Assoc. Amer. Geogr.,* **98,** 521–552, doi:10.1080/00045600802046387.

Wang, Y., C. L. Klipp, D. M. Garvey, D. A. Ligon, C. C. Williamson, S. S. Chang, R. K. Newsom, and R. Calhoun, 2007: Nocturnal low-level-jet-dominated atmospheric boundary layer observed by a Doppler lidar over Oklahoma City during 2003. *J. Appl. Meteor. Climatol.,* **46,** 2098–2109, doi:10.1175/2006JAMC1283.1.

Webb, E. K., G. I. Pearman, and R. Leuning, 1980: Correction of flux measurements for density effects due to heat and water vapour transfer. *Quart. J. Roy. Meteor. Soc.,* **106,** 85–100, doi:10.1002/qj.49710644707.

Whiteman, C. D., X. Bian, and S. Zhong, 1997: Low-level jet climatology from enhanced rawinsonde observations at a site in the southern Great Plains. *J. Appl. Meteor.,* **36,** 1363–1376, doi:10.1175/1520-0450(1997)036<1363:LLJCFE>2.0.CO;2.

Wulfmeyer, V., S. Pal, D. D. Turner, and E. Wagner, 2010: Can water vapour Raman lidar resolve profiles of turbulent variables in the convective boundary layer? *Bound.-Layer Meteor.,* **136,** 253–284, doi:10.1007/s10546-010-9494-z.

Wyngaard, J. C., 2010: *Turbulence in the Atmosphere*. Cambridge University Press, 393 pp.

Yurganov, L., W. McMillan, C. Wilson, M. Fischer, and C. Sweeney, 2010: Carbon monoxide mixing ratios over Oklahoma between 2002 and 2009 retrieved from Atmospheric Emitted Radiance Interferometer spectra. *Atmos. Meas. Technol.,* **3,** 1319–1331, doi:10.5194/amt-3-1319-2010.

Zhong, S., J. D. Fast, and X. Bian, 1996: A case study of the Great Plains low-level jet using wind profiler network data and a high-resolution mesoscale model. *Mon. Wea. Rev.,* **124,** 785–806, doi:10.1175/1520-0493(1996)124<0785:ACSOTG>2.0.CO;2.